arXiv:0712.2458v2 [astro-ph] 15 Dec 2008

Spitzer IRS Observations of Class I/II Objects in Taurus: Composition and Thermal History of the Circumstellar Ices

G. Zasowski[1], F. Kemper[2,1], Dan M. Watson[3], E. Furlan[4,5], C.J. Bohac[3], C. Hull[1], and J.D. Green[3]

ABSTRACT

We present observations of Taurus-Auriga Class I/II protostars obtained with the Spitzer InfraRed Spectrograph. Detailed spectral fits to the 6 and 15.2 micron ice features are made, using publicly-available laboratory data, to constrain the molecular composition, abundances, and levels of thermal processing along the lines of sight. We provide an inventory of the molecular environments observed, which have an average composition dominated by water ice with ∼12% CO_2 (abundance relative to H_2O), $\gtrsim$2-9% CH_3OH, ∼14% NH_3, ∼3% CH_4, ∼2% H_2CO, ∼0.6% HCOOH, and ∼0.5% SO_2. We find CO_2/H_2O ratios nearly equivalent to those observed in cold clouds and lines of sight toward the galactic center. The unidentified 6.8 micron profiles vary from source to source, and it is shown to be likely that even combinations of the most common candidates (NH_4^+ and CH_3OH) are inadequate to explain the feature fully. We discuss correlations among SED spectral indices, abundance ratios, and thermally-processed ice fractions and their implications for CO_2 formation and evolution. Comparison of our spectral fits with cold molecular cloud sight-lines indicates abundant prestellar ice environments made even richer by the radiative effects of protostars. Our results add additional constraints and a finer level of detail to current full-scale models of protostellar and protoplanetary systems.

---

[1] Department of Astronomy, PO Box 400325, University of Virginia, Charlottesville, VA 22904-4325: gailis@virginia.edu, chat.hull@gmail.com

[2] Jodrell Bank Centre for Astrophysics, University of Manchester, Manchester, M13 9PL, UK: Ciska.Kemper@manchester.ac.uk

[3] Department of Physics and Astronomy, University of Rochester, Bausch & Lomb Hall, PO Box 270171, 500 Wilson Blvd, Rochester, NY 14627-0171: dmw@pas.rochester.edu, joel@pas.rochester.edu, urgradcb@gmail.com

[4] NASA Astrobiology Institute and Department of Physics and Astronomy, UCLA, 430 Portola Plaza, Los Angeles, CA 90095: furlan@astro.ucla.edu

[5] Current address: Jet Propulsion Laboratory, Caltech, Mail Stop 264-767, 4800 Oak Grove Drive, Pasadena, CA 91109

Subject headings: stars: pre-main sequence — ISM: abundances — ISM: molecules — infrared: ISM — astrochemistry

1. INTRODUCTION

The chemical and thermal evolution of protostellar environments affects the spectral appearance of ices observed in the sequential stages of pre-main-sequence evolution (e.g. Willner et al. 1982; Gerakines et al. 1999; van Dishoeck 2006). The presence of the ice absorption features is often easily recognized, with the most common ones in the mid-infrared wavelength range found at 6.0, 6.8, and 15.2 μm, but the exact feature shapes depend strongly on the composition of the ice as determined by the initial condensation and subsequent thermal processing and UV irradiation. Mixing ices can cause wavelength shifts in the resonances of the individual components within the ice matrix (e.g. Ehrenfreund et al. 1999; Palumbo & Baratta 2000; Öberg et al. 2007), and differences in lattice structure caused by either radiation damage or thermal processing are spectroscopically identifiable (e.g. Hagen et al. 1981; Moore & Hudson 1992; Maldoni et al. 1998; Kouchi & Kuroda 1990).

The initial reservoir of star formation material, the diffuse ISM, is extremely ice-poor (e.g. Gillett et al. 1975; Whittet et al. 1997). It is not dense enough to shield its dust grains, upon which ices condense (e.g. Tielens & Allamandola 1987), from incident destructive photons. Only when cold molecular clouds of high density ($n_H \gtrsim 10^4$ cm^{-3}) are formed can interstellar ices survive and be observed. In the Taurus molecular cloud, for example, a well-known seat of starbirth, ices are observed towards background stars even in quiescent regions unaffected by the newly-formed stars (e.g. Bergin et al. 2005; Knez et al. 2005; Whittet et al. 2007). These studies reveal absorptions attributable to H_2O, CO, and CO_2, as well as some less-constrained absorptions (e.g. the still unidentified band at 6.8 μm) due to presumably more complex species. The ice bands observed towards these field stars are smooth, indicating amorphous and unprocessed compounds, and low upper limits can be placed on some species created by UV radiation (e.g. "XCN"; Gibb et al. 2004). These observations support the theory that molecular cloud ice chemistry is dominated by efficient cold grain surface reactions. The presence of larger complex molecules (such as HCOOH, which can be formed at low temperatures; Keane 2001) demonstrates the potential complexity of these reactions and indicates that protostars are born into a pre-enriched chemical environment.

Surveys of deeply embedded young stellar objects (YSOs) reveal a limited range of thermal processing, indicative of differences in YSO environment and temperature (e.g. Gerakines et al. 1999; Gibb et al. 2004). Studies of less-extinguished protostars (Class I in the classification of Lada 1987) show evidence of enhanced complex molecule formation

(H_2CO, XCN, OCS, PAHs [polycyclic aromatic hydrocarbons]), ice crystallization, further thermal annealing, and ice matrix segregation (see e.g. Alexander et al. 2003; Keane et al. 2001; Ehrenfreund et al. 1998; Watson et al. 2004; Gibb et al. 2004; Boogert et al. 2004).

Finally, the least embedded Class II objects have seemingly accreted or dissipated most of their cold natal envelopes and have heated the outer layers of their dust disks above the sublimation temperature of astrophysical ices. These objects tend to show silicate dust *emission*, PAH emissions, and weak or nonexistant ice signatures (e.g. Forrest et al. 2004; Furlan et al. 2006), though some Class II edge-on systems have ice absorptions arising from the cold disk midplane (e.g. Pontoppidan et al. 2005; Furlan et al. 2008).

Differences in chemical and physical structure exist between YSOs with masses either above or below a few $M_\odot$ (van Dishoeck 2003). Some of these dissimilarities may be attributed to observational biases (low-mass YSOs are generally closer and can be better resolved), but others are likely to be dependent on the intrinsic nature of the object (e.g. the role of shocks, core temperature, and infall timescales). For example, low-mass YSO studies claim higher abundances of CO_2, relative to H_2O (Boogert et al. 2004; Pontoppidan et al. 2008) and amorphous silicate dust (Watson et al. 2004), than surveys of more massive YSOs. This paper focuses on the relatively underexplored categories of low-mass Class I protostars and Class I/II transition objects (henceforth both groups will be collectively referred to as Class I/II objects) with ice absorptions by analyzing mid-infrared spectroscopy of 16 Taurus-Auriga YSOs (<1-3 Myr old; White & Ghez 2001), observed with the InfraRed Spectrograph (IRS; Houck et al. 2004) on board the Spitzer Space Telescope (Werner et al. 2004). Our sample overlaps slightly with that of the extensive recent work by the *c2d* team (e.g. Boogert et al. 2008; Pontoppidan et al. 2008; Öberg et al. 2008), and we indicate differences in our approach and findings throughout this paper. This study helps complete our view of the ice evolutionary sequence from cold molecular clouds through warmer environments with protoplanetary disks. These low-mass, possibly early solar analogs are essential pieces to the puzzle of solar system formation.

Section 2 contains a short description of the sample, observations, and data reduction. In Section 3 we describe how the ice features are identified, isolated, and analyzed, and in Section 4 we look at trends seen in the feature optical depths. In Section 5 we derive the composition of the carriers of the primary ice absorptions and evaluate candidates for some of the less constrained features. In Section 6 we discuss composition and spatial distribution of the ices and place our observations in the context of pre-main-sequence evolution.

2. OBSERVATIONS

2.1. Target Sample Description

The Taurus-Auriga dark cloud is a nearby (d $\sim$ 140 pc; Bertout et al. 1999), low density ($n_* \sim$ 1-10 pc^{-3}; Gomez et al. 1993) star forming region containing predominantly young, low-mass protostars. It provides an opportunity to study closely low-mass star formation unaffected by the shocks and strong UV radiation associated with more massive protostars. Based on IRAS 25 and 60 μm photometry, an extensive sample of Class I/II objects was selected from the list by Kenyon & Hartmann (1995) and observed with Spitzer's IRS (Section 2.2). From this sample we chose for analysis the subset of 12 Class I and 4 Class II objects (as classified in Kenyon & Hartmann 1995) with distinct ice features in regions of unsaturated, well-calibrated data. The IRAS spectral energy distribution (SED) points used in the original selection are insufficient to determine system inclination, but modeling by Furlan et al. (2008) indicates that our smaller sample spans a wide range of disk inclination angles, from nearly edge-on to face-on systems.

For comparison, we include a secondary sample comprising observations of Taurus and Serpens cloud field stars—Elias 16, Elias 13, and CK 2—as well as of the Class 0 protostars CepE-MM and L1448 IRS 2 (AOR IDs 3623680, 3620352). We also include data from the line of sight towards the W3(OH) star formation region, which probes part of the foreground W3 molecular cloud (AOR ID 3566336).

2.2. Observational Procedure and Data Reduction

Our sample was observed with Spitzer's IRS as part of the *IRS Disks* project (PI: J. Houck & D. Watson; PID 2) during guaranteed time awarded to the IRS instrument team (2004 February-March). All of our targets were observed using the full 5–37 μm wavelength coverage, combining either the Short Low and Long Low (SL, LL; 5.2-14 μm, 14-38 μm; $\lambda/\Delta\lambda \sim 90$) modules on the IRS, or the SL with the Short High and Long High (SH, LH; 10-19 μm, 19-37 μm; $\lambda/\Delta\lambda \sim 600$) modules, depending on the expected flux levels.

Most (12) of the objects were observed using a small spectral map (3×2) rather than a single pointing; this strategy avoids the need for pointing peak-ups and allows, in principle, for a better reconstruction of the spectrum in cases of small mispointings. The three-step sequence was carried out in the dispersion direction, with the steps separated by three quarters (for the SL module) or one half (for the other modules) of the slit width. The two-step sequence corresponds to the normal IRS nod distance of one-third the slit length.

The other 4 objects were observed in the IRS staring mode, using only the two nods along the slit. Observational details of all our Class I/II targets are listed in Table 1.

We analyzed data from pipeline version S13, using the SMART package (Higdon et al. 2004). The standard *IRS Disks* reduction procedures, as well as any spectra requiring special treatment, are described in Furlan et al. (2006) and Furlan et al. (2008).

The uncertainty in each wavelength bin is taken to be half of the nod difference in flux level, except where this value is smaller than 1% of the flux. In those cases, the uncertainties are taken to be 1% of the flux in order to prevent underestimation. We estimate an absolute spectrophotometric accuracy of 5-10%.

For the field stars, we use the previously published data for Elias 16 (Bergin et al. 2005) and Elias 13 and CK 2 (Knez et al. 2005), without re-reducing the data.

2.3. IRS Spectra Description

In Figure 1, we show the IRS spectra of the 16 Class I/II stars in our sample. The YSO mid-infrared spectra are dominated by broad solid state resonances, particularly those at 6.0, 6.8, 9.7, and 15.2 μm. Additional, but less pronounced, features are visible in some spectra at 7.7 μm and as a broad band centered at 18 μm. Silicates are responsible for the broad 9.7 and 18 μm features, which can occur in either absorption (e.g. L1551 IRS 5), emission (e.g. IRAS 04108+2803A), or both.

The 6.0 μm feature is primarily due to the O-H bending mode of water ice, while the 6.8 μm feature remains largely unidentified, with CH_3OH and NH_4^+ (among others) as suggested carriers. The 7.7 μm absorption is generally attributed to solid CH_4, and the 15.2 μm band is due to the O-C-O bending mode of solid CO_2. A complete inventory of absorption features identified in our spectra is contained in Table 2.

Spectra for W3(OH) and the Class 0 objects (Figure 2) contain many of the same features.

3. METHODS

3.1. Isolating the IR Features and Determining Optical Depths

3.1.1. YSO Spectra

The optical depth, τ, and shape of the individual absorption features under consideration are extracted from the astronomical spectra using a mathematical continuum fit. We make a cubic spline fit to the ∼5-20 μm continuum of each spectrum using the following relatively feature-free regions: bluewards of the 6 μm H_2O feature; between the unidentified 6.8 μm feature and the onset of the 9.7 μm silicate band; between the red wing of the silicate band (∼14.5 μm) and the 15.2 μm CO_2 feature; and redwards of the CO_2 feature—while ensuring that none of the feature wings are included in the continuum. We calculate the optical depth in the spectral features using $F_\lambda = F_{\lambda,cont} e^{-\tau_\lambda}$.

Because the 9.7 μm silicate feature is highly complex, and detailed modeling of the silicate mineralogy is beyond the scope of this paper, accurate extraction of ice features blended with the 9.7 μm silicate complex (e.g. those of CH_3OH, NH_3, and H_2O) is impractical. However, the 11-13 μm H_2O libration band and the 18 μm absorption feature in particularly silicate-rich spectra are much broader and shallower than the 15.2 μm ice absorption they overlap, so we can treat these shapes as pseudo-continua in order to isolate the CO_2 ice absorption.

Additional steps are needed to extract small features in the 7-8 μm range. The wide variation in 6.8 μm and silicate absorption profile wings requires that each spectrum be treated individually. For objects not affected by the silicate feature bluewards of 8 μm, a straight-line continuum (∼7.1-8 μm) is imposed to isolate any features. For objects affected by both the 6.8 and the 9.7 μm features, two straight-line continua are imposed: one from ∼7.1-7.5 μm and one from ∼7.5-8 μm (Figure 3).

3.1.2. Laboratory Spectra

We use laboratory data from the Leiden University ice analog databases[1] (Gerakines et al. 1995, 1996; Ehrenfreund et al. 1996, 1999; van Broekhuizen et al. 2006) to identify the composition and apparent temperatures of the ices seen in our targets. In order to provide a direct comparison between the feature optical depths measured in the laboratory and those observed in the astronomical spectra, we removed a straight-line continuum from the laboratory data. For the wavelength ranges of interest, optical depths calculated using a straight-line continuum differ, on average, by less than half of a percent from those calculated using a more complicated cubic spline one. The wavelengths of the baseline ends are generally equal to the continuum points used in the astronomical spectra's spline fitting, with an occasional slight shift to ensure feature wings are excluded from the continuum. In Figure 4 we show the range of abundances contained in the Leiden databases' non-irradiated H_2O:CH_3OH:CO_2 mixtures (T=10-185K, all circles); note that this plot does not represent the fraction of the database comprising other molecules (e.g. CH_4 and H_2OH) or UV-irradiated mixtures.

---

[1] http://www.strw.leidenuniv.nl/∼lab/databases/databases.htm

The temperatures given in this paper, except where otherwise noted, refer to laboratory conditions. Interstellar temperature barriers for crystallization, sublimation, and other physical processes are lower than their laboratory counterparts, due to the lower pressure and longer interaction timescales in interstellar space (e.g. Boogert et al. 2000). Assumptions about particle shapes have not been applied to the laboratory spectra used in this broad analysis, and such corrections would in any case be inappropriate for the annealed inhomogeneous mixtures used (Gerakines et al. 1999).

3.2. Spectral Fitting

To confirm the validity of using laboratory spectra to model circumstellar material, we estimate the total extinction A_V along the line of sight towards our YSOs using $A_V/\tau_{Si} \sim 17$ (Rieke & Lebofsky 1985). We find $A_V \sim$ 3-34 for our total sample—and $A_V \sim$ 6-34 for those objects without clear signs of dust emission contaminating the absorption feature—compared with the average extinction of $A_V \sim$ 1-5 toward Taurus association stars (Myers et al. 1983). In addition, recent work has shown that in dense regions, this relation with a given τ_{Si} substantially underestimates A_V (Whittet et al. 1988; Chiar et al. 2007), so the total circumstellar extinction is likely to be even higher.

Thus, we assume that the foreground absorption towards the Taurus region is relatively low and that the spectral ice features result from material in the circumstellar environment. In contrast with a least-components type of analysis (e.g. Boogert et al. 2008; Pontoppidan et al. 2008), we determine the ice composition and column densities of the circumstellar ice by fitting linear combinations of laboratory data to the observed IRS spectra. With the laboratory data described in Section 3.1.2, detailed spectral fitting is performed on the 6.0 and 15.2 μm features using a standard χ^2-minimization technique. The equation solved is

$$\tau(\lambda) = \sum a_i \tau_{lab,i}(\lambda), \tag{1}$$

where the scale factors a_i of each component are the free parameters in the fit. To compare goodness-of-fit among various combinations, we use χ^2_ν, the reduced χ^2 parameter. This is defined as χ^2_ν=$\chi^2/(n-m)$, where n is the number of spectral data points and m is the number of free parameters in the fit. Traditional statistics require $\chi^2_\nu \sim 1$ for an acceptable fit, but our values are often significantly larger or smaller. Artificially small χ^2_ν values can be caused by uncertainty overestimation or by poor signal-to-noise. Large values may be a result of uncertainty underestimation, unknown uncertainties in the laboratory spectra, or the existence of components not included in the fits. Therefore χ^2_ν comparisons may be made to determine the best laboratory fit to a single spectrum; however, comparisons of goodness-of-fit among different YSO spectra are not necessarily valid. Quantities derived using a fitted spectral feature (e.g. processed fractions, column densities) are calculated using an average of all fits for that feature with a χ^2_ν within 20% of the minimum.

3.3. Column Densities

To calculate column densities along the lines of sight to the YSOs, we use the relation (e.g. Alexander et al. 2003)

$$N(cm^{-2}) = \frac{\sum \tau_\lambda \Delta\lambda}{\lambda^2_{peak} A}, \tag{2}$$

where $\Delta\lambda$ is the wavelength bin size, λ_{peak} is the wavelength of the feature's peak optical depth, and A (cm molec^{-1}) is the band strength as determined in the laboratory.

3.4. SED Spectral Index

To provide better resolution in evolutionary status than the simple Lada (1987) classification, we use the spectral index α (e.g. Kenyon & Hartmann 1995):

$$\alpha \equiv \frac{d \log \lambda F_\lambda}{d \log \lambda} \sim \frac{\log \lambda_2 F_{\lambda_2} - \log \lambda_1 F_{\lambda_1}}{\log \lambda_2 - \log \lambda_1}, \tag{3}$$

where we choose λ_1 and λ_2 to lie within well-calibrated and nearly-featureless parts of the spectrum but as much separated as possible (i.e. $\lambda_1 = 7$ μm and $\lambda_2 = 30$ μm; Table 3). The slope of this section of the spectrum depends upon a variety of factors, including disk radius, total envelope density, outflow cavity opening angle, and inclination angle. With the exception of inclination angle, all of these factors depend upon the total dust column density in such a way that more dust produces a steeper SED slope, and models demonstrate that inclination angle effects are generally less significant than these other factors (Furlan et al.

2008). Thus small values for the spectral index α indicate a relatively blue or exposed stellar object, but with increasing α the spectrum becomes redder, indicating the YSO is more heavily embedded in dust.

4. OPTICAL DEPTH TRENDS

In Figure 5, we show correlations in the optical depths of the three strongest absorptions attributed to ices (at 6.0, 6.8, and 15.2 μm) in our YSO sample. Clearly, the 6.0 and 6.8 μm features are very closely correlated, with linear Pearson correlation coefficient $r = 0.96$ (Figure 5a). The peak ratio is $\tau_{6.8}/\tau_{6.0} \sim 0.96\pm0.03$, and the straight-line fit passes within 0.01 of the origin. Since the 6.0 μm band is primarily attributed to the bending mode of H_2O, this correlation indicates that the carrier(s) of the 6.8 μm band forms and evolves in a similar, polar environment.

There is a looser correlation between the 6.0 μm and the 15.2 μm optical depths in our YSOs ($r = 0.7$, Figure 5b), resulting in a wider ratio range $\tau_{6.0}/\tau_{15.2} \sim 0.43$-1.65. When the same ratios are calculated for the laboratory spectra, though the spread is even wider (0.01-3.6), only a small fraction fall within the range defined by the YSOs (Figure 4, filled circles); the 15.2 μm CO_2 feature is generally much stronger than the 6.0 μm water ice feature, independent of temperature. Mixtures dominated by H_2O provide most of the closest matches. In addition, there are two lab mixtures of nearly 1:1:1 H_2O:CH_3OH:CO_2 abundances (center of Figure 4) which have $\tau_{6.0}/\tau_{15.2}$ ratios comparable to the YSO ones but only after they have been heated to high temperatures (T $\gtrsim$ 125 K), nearing the ice sublimation points. The Leiden database has a scarcity of water-rich, CO_2-poor ($\lesssim$20%) H_2O:CH_3OH:CO_2 mixtures in the temperature range 10-180 K, though based on this comparison, these compositions appear to be astronomically relevant. Because of the undersampling of compositions in this range, we are not able to constrain the ice composition well from the $\tau_{6.0}/\tau_{15.2}$ ratio alone.

Despite being closely correlated with $\tau_{6.0}$, the 6.8 μm peak optical depth is even less correlated with the 15.2 μm depths ($r = 0.56$, Figure 5c). This indicates that much of the inherent scatter in the $\tau_{6.8}/\tau_{6.0}$ ratio is due to variations in the 6.8 μm feature among different lines of sight.

5. SPECTRAL FEATURE ANALYSES

In order to set more accurate constraints on the ice properties than feature-strength analysis provides, we perform spectral fitting and detailed analysis of the most prominent features.

5.1. The 6.0 μm Feature

Each YSO spectrum is fitted over the wavelength range 5.4-6.3 μm using the method described in Section 3.2 and the component set listed in Table 4. An example result is shown in Figure 6, and the total sample residuals, after subtraction of the 6 μm components, are shown in Figure 8. Due to overlap with the unidentified 6.8 μm feature, the range beyond 6.3 μm was excluded in order to avoid imposing artificial structure on any fit residuals. These fits focus on identifying the constituents of the 6.0 μm feature—H_2O, H_2CO, HCOOH, and NH_3, as described in the following subsections. This suite of species is similar to that employed by Boogert et al. (2008) to explain their extracted component set C1-5.

Either noise or saturation of the absorption bands in the background star/Class 0 sample prevents detailed spectral fitting of the 6 μm features, so we scaled a pure H_2O (10 K) spectrum to match the peak optical depth at 6.0 μm in order to calculate $N(H_2O)$ (Table 8). The shape of the 6 μm W3 spectrum is too irregular to be reasonably fit with a solid H_2O lab spectrum in this manner.

5.1.1. H_2O

Water is the least volatile and most abundant of the ices typically found along protostellar lines of sight. The mid-infrared spectrum offers three strong features of water ice: narrow ones at 3.1 and 6.0 μm, and a broad ($\lambda \sim$ 11-20 μm) feature peaking at 13 μm. To turn these profiles into water ice column density is somewhat problematic in each case. The 3.1 μm ice feature is generally regarded as the cleanest measure of H_2O ice column density (e.g. Tielens et al. 1984). However, inconvenient gaps in the spectrum transmitted by Earth's atmosphere make it difficult to determine the continuum on the short wavelength side of this feature in ground-based observations, which would be the source of most of the comparisons we could make to our data. In addition, rather significant extinction and scattering near 3 μm are inevitably associated with protostars and can affect the profile of the water ice feature. Futhermore, this may lead to the bulk of the 3 μm background continuum taking a significantly different path through the protostellar envelope than that which gives rise to the longer-wavelength features. The latter effect would be rather more serious in systems viewed closer to edge-on, such as IRAS 04169+2702 and DG Tau B.

Extinction at 6 μm is similar to that at 13 μm, and both are significantly smaller than that at 3 μm (extinction in magnitudes smaller by factors of $\sim$ 2-3; Mathis 1990; Indebetouw et al. 2005). Thus the optical paths sampled at 6 and 13 μm, and the ice column densities derived, should be similar and may be more characteristic of the line of sight to the embedded protostar than is the case at 3 μm. In observed spectra, the 6 μm feature is the easiest of the three to analyze, as there are fewer problems in determination of the continuum. However, the depth and profile of the 6 μm feature are possibly influenced by absorption from species other than water ice, as shown, for example, by Boogert et al. (2008). The 13 μm water ice libration feature is broad and overlaps many other absorptions, including the loosely-constrained 9.7 μm silicate feature, so its optical depth and feature shape are hard to measure precisely.

Taking account of all of these difficulties, we choose to measure water ice column density with the 6 μm feature, and check against the possibility of substantial "contamination" from other species using the 13 μm feature. To calculate the H_2O column density, we use the 6.0 μm feature fit results along with Equation 2 (summed over λ=5.5-7 μm), with a band strength of A_{H_2O}=1.2$\times$10^{17}cm molec^{-1} for the T = 50 K water ice components and A_{H_2O}=1.3$\times$10^{17}cm molec^{-1} for the T = 120 K one. These values pertain to pure H_2O ice, though they are also suitable for apolar dilutant concentrations of $\lesssim$30% (Gerakines et al. 1995). We note that the derived column densities $N(H_2O)$ (Table 5) may in some cases represent upper limits, as the overall composition of the 6 μm feature is still a source of discussion (e.g. Gibb et al. 2004; Boogert et al. 2008). However, as we will see below, the consistency of these results with those from 13 μm features in our spectra indicates that the contribution of unaccounted-for species at 6 μm is rather small compared to that of water ice. In general, our values of water ice column density are somewhat larger than those derived for the same objects from the 3.1 μm feature (e.g. Boogert et al. 2008), and tend to depart more the closer the object is to an edge-on view, so the differences may in part be due to the expected differences between the light paths viewed at the two wavelengths.

To look for signs of additional ice components with features near 6 μm that are not resolved spectrally from the water-ice feature, we have measured the 11-20 μm solid H_2O absorption in the nine targets for which the 10 μm silicate feature is most deeply in absorption. To do so, we followed a procedure similar to that by Boogert et al. (2008). From a low-order polynomial fit to the continuum, constrained to follow the spectrum at 5.3-5.6 and 30-35 μm, we determined the total optical depth in the 8-30 μm range. To this we "fit" the profile of interstellar silicate absorption, exemplified by the galactic center source GCS 3 (Kemper et al. 2004) and constrained to match the observed spectrum at 9.9-10.1 μm and 23-30 μm. Since this interstellar silicate profile may not be fully applicable to circumstellar silicates, this step introduces additional uncertainty. Subtraction of the resulting profile from the optical depth spectrum reveals the water ice libration absorption, peaking at ~13 μm, and interrupted at 15.2 μm by the CO_2 ice feature. We measured from such results the peak optical depth in this water ice feature around 13 μm. By small variation of the wavelengths at which the continuum and silicate profile were constrained to follow the spectrum, we estimated the uncertainty in the peak optical depth. Because the shape of this very broad water feature is more sensitive to both the continuum and silicate profile fits than is the peak optical depth, the corresponding water ice column density is considerably more uncertain. In Figure 7, the values for peak optical depth are plotted against the column density $N(H_2O)$ derived from the 6 μm feature as described above. Evident in Figure 7 is a good correlation between the 13 and 6 μm water signatures, with Pearson's $r = 0.74$. That the correlation is tight indicates that, if an additional ice component is significant at 6 μm, its abundance relative to water ice must be essentially constant.

5.1.2. H_2CO and HCOOH

Many of the objects in our sample have additional absorptions centered around ~5.8 μm that can be well-fit by a combination of H_2CO (formaldehyde) and HCOOH (formic acid) ices. Solid H_2CO is observed in many protostellar systems (e.g. Keane et al. 2001; Gibb et al. 2004) and plays an important role in the production of complex organic molecules (Schutte et al. 1993). H_2CO is difficult to detect independently in YSO Spitzer spectra; its 3.47 μm C-H stretch feature is beyond the wavelength range of the IRS, and its weaker 6.68 μm C=O stretch feature is blended with the 6.8 μm absorption, itself not well understood. The H_2CO column densities (Table 5) are derived using the observed integrated optical depth of the 5.8 μm feature (as determined from the spectral fits) and a band strength of A_{H_2CO}=9.6×10^{-18}cm molec^{-1} (Schutte et al. 1993).

Solid and gas-phase HCOOH has been detected in both low- and high-mass star-forming regions (e.g. Cazaux et al. 2003; Schutte et al. 1999; Bottinelli et al. 2004; Remijan et al. 2004; Keane et al. 2001). Within the IRS wavelength range, there are solid-state HCOOH absorptions at 5.8 and 7.2 μm, and several in the 8-11 μm range (Bisschop et al. 2007). The latter ones are blended with the 9.7 μm silicate complex, but the 7.2 μm band, though intrinsically ~4 times weaker than the 5.8 μm resonance, is detectable and indeed is tentatively identified in 6 of our 16 objects (Section 5.3). We have derived HCOOH column densities (Table 5) by integrating the observed optical depth of the 5.8 μm feature (as determined from the spectral fits) and using a band strength of A_{HCOOH}=6.7×10^{-17}cm molec^{-1} (Maréchal 1987).

5.1.3. NH$_3$

Solid NH_3 (ammonia) has mid-infrared features at 6.15 μm and 9.3 μm (e.g. Sandford & Allamandola 1993), blended with the 6 μm water ice and 9.7 μm silicate features, respectively. The effect on the 6 μm H_2O feature is negligible until the NH_3 concentration reaches ∼9% (Keane et al. 2001). At higher concentrations, an excess appears around 6.15 μm on the red side of the 6 μm band in laboratory spectra, which fits well the broad 6 μm feature observed in many of our YSO spectra. Analyses of the 9 μm inversion mode resonance by Lacy et al. (1998) and Gibb et al. (2000) indicate that circumprotostellar NH_3 exists primarily in an H_2O-dominated matrix. Therefore, an H_2O:NH_3 (1:0.2) mixture, rather than pure NH_3, is used in the spectral fits. Because no satisfactory band strength measurements for NH_3 in such a mixture exist, the upper limit NH_3 column densities (Table 5) are estimated by using the band strength of pure water ice for the H_2O:NH_3 mixture and extrapolating the column density of NH_3 based on its fractional abundance in the final fit.

5.1.4. PAHs

After contributions due to H_2O, H_2CO, HCOOH, and NH_3 are subtracted, small residuals in the 6.1-6.4 μm range, varying in strength, shape, and peak position, are observed in 11 of the sample's 16 YSOs (Figure 8). PAH absorption has been suggested as a candidate for the 6.2-6.3 μm feature observed in many massive protostars (Schutte et al. 1996). Using the average interstellar PAH spectrum compiled by Hony et al. (2001) as a reference, we examined the peak position and widths of the YSO residuals. Of the objects within our sample with excess absorptions peaking between 6.2 and 6.3 μm, only three (IRAS 04361+2540, DG Tau B, and HL Tau) have an excess with a width similar to that seen in the PAH spectrum, and none of these three match the PAH feature in shape and peak position. Though the PAH relative band strengths often depend upon molecular environment and ionization level, the broad 7.5-9 μm complex and the 6.2 μm feature are consistently observed at comparable strength in astronomical environments (Hony et al. 2001), yet we find no correlation in the YSO spectra between the 6.2 and 7.7 μm optical depths—the ratios are scattered between 0 and 7.5. Moreover, the prominent but narrow PAH peak at 11.3 μm (consistently ∼1.4× as strong as the 6.2 μm peak; Chan et al. 2000; Hony et al. 2001) and the lesser ones at 12.7, 13.5, and 14.3 μm are not observed in the YSO data. Thus in agreement with Keane et al. (2001), we find it unlikely that PAHs contribute significantly around 6.2-6.3 μm.

5.2. The 6.8 μm Feature

Though the 6.8 μm interstellar absorption band was discovered nearly 30 years ago (Puetter et al. 1979), its identification remains ambiguous and inconclusive. Species ranging from hydrocarbons to alcohols to carbon dust have been proposed to contribute to the feature in a variety of sources (see Keane et al. 2001). Here we focus on CH_3OH and NH_4^+—the candidate carriers most commonly accepted as explaining at least part of the absorption (e.g. Boogert & Ehrenfreund 2004).

5.2.1. CH_3OH

The position of the 6.8 μm feature coincides with the C-H deformation mode of alcohols, and of these, methanol is the most likely to be found in interstellar abundance. Theoretical models of ice processes predict the creation of solid methanol through the sequential hydrogenation of CO ice which has been accreted from the gas phase onto dust grains (Tielens & Charnley 1997). The presence of methanol ice in interstellar and protostellar environments is observationally supported by detection of its own resonances—e.g. the C-H stretching mode at 3.54 μm (Grim et al. 1991) and the C-O stretch at 9.8 μm (Gibb et al. 2000)—as well as by signatures of its interactions with other molecules (especially CO_2; e.g. Ehrenfreund et al. 1998).

Our sample spectra do not contain the NIR wavelengths of CH_3OH's multiple stretching modes, and the 9.8 μm resonance is blended with the silicate absorption. However, constraints on the CH_3OH abundance can be derived using the 15.2 μm CO_2 band, as the interaction of CH_3OH with CO_2 changes the feature shape near 15.4 μm (Sections 5.4 and 6.1). The relative strength of the 15.4 μm shoulder implies that at most 50% of the 6.8 μm feature is due to CH_3OH in a CO_2 matrix, although CH_3OH unmixed with CO_2 could be present to provide additional absorption at 6.8 μm. Since CH_3OH is thought to form in a hydrogenated environment, the assignment of at least part of the 6.8 μm absorption to this molecule is then supported by the close correlation of the 6.0 and 6.8 μm optical depths (Section 4).

5.2.2. NH_4^+

The NH_4^+ ion was proposed as the carrier of the 6.8 μm band by Grim et al. (1989), and since then, this proposal has achieved varying levels of success (e.g Schutte et al. 1996; Keane et al. 2001; Schutte & Khanna 2003). The ion can be produced in the laboratory by the acid-base reaction HNCO + $NH_3 \rightarrow OCN^- + NH_4^+$ (Keane 1997) or in UV-irradiated H_2O:CO:NH_3 mixtures (as in Figure 8).

NH_4^+ has expected counter-ion features at 4.62 μm (OCN^-) and 6.3 and 7.41 μm ($HCOO^-$, produced by photolysis). The 4.62 μm feature does not fall within the IRS wavelength coverage, and the 7.41 μm signature is too weak to be conclusively identified in our data. However, some of our sample objects do have a small excess absorption near 6.3 μm (Section 5.1.4), which is unlikely to be attributable to PAHs. It may instead be due to $HCOO^-$, indicating photolysis and subsequent warming of a polar ice containing NH_3. We use the ratios of the laboratory 6.3 μm ($HCOO^-$) and 6.8 μm (NH_4^+) peaks ($\tau_{6.8}/\tau_{6.3} \sim 1.7$ after the H_2O feature is removed), along with the equivalent widths of the YSO and laboratory features, to estimate the NH_4^+ contribution to the 6.8 μm feature. Using this method, we find that, within our sample, 6-58% of the 6.8 μm feature can be attributed to NH_4^+ (HL Tau is an outlier whose particularly large 6.3 μm excess indicates $\lesssim$91% of its 6.8 μm feature may be due to NH_4^+ using this method).

5.2.3. Fits and Summary

Figure 8 shows a comparison of the 6.8 μm features, after subtraction of the 6 μm contributors, with a variety of 6.8 μm candidate laboratory spectra, all rebinned to the resolution of the observations. The bottom two lab spectra (Lab B and C) have CH_3OH/H_2O abundance ratios of 100 and 0.1, and the gray vertical lines indicate the peak positions of these mixtures. The relative amount of methanol present affects the peak substructure. While in some cases the YSO peak positions and relative strengths closely resemble the laboratory data (e.g. IC 2087 IR and IRAS 04239+2436), in others there is no correlation at all (e.g. IRAS 04169+2702). The abundance of CH_3OH (relative to H_2O) has been found to vary by almost an order of magnitude among different protostellar lines of sight (e.g Pontoppidan et al. 2003; Gibb et al. 2004), which may partly explain the observed variety of peak substructures.

The top laboratory spectrum in Figure 8 (Lab A) is a H_2O:CO:NH_3 deposit, irradiated to create NH_4^+ and subsequently warmed from 10 to 165 K. The irradiated spectrum at 10 K peaks 0.1 μm bluewards of our sample's bluest feature; in order to align with any of the observed profiles, the irradiated mixture must be heated to near the H_2O sublimation temperature, as the sublimation appears to cause the redward peak shift (Schutte et al. 1996). Moreover, the width of the NH_4^+ feature is too narrow (~0.25 μm) to account for the entire 6.8 μm feature widths observed towards each YSO (average ~0.4 μm). Even if multiple NH_4^+ laboratory spectra at various temperatures are combined in order to reproduce the observed feature width, the resultant peak position remains too blue to match the YSO data.

Noting that many of the YSO 6.8 μm features share characteristics with the profiles of both CH_3OH (triple peaks, 7 μm shoulder) and NH_4^+ (asymmetric peak near 6.75 μm), we attempted fitting them with a combination of the laboratory components. While no remarkably good fits were achieved, there emerged a general trend that equal contributions from NH_4^+ and from CH_3OH in a water-dominated matrix, with varying amounts of nearly-pure CH_3OH intermixed, came closest to reproducing many of the YSO feature width-to-depth ratios (i.e. mixtures of irradiated NH_3, $CH_3OH/H_2O \sim 0.1$, and $CH_3OH/H_2O \sim 100$ in the approximate ratios 1:1:0 to 1:1:1). However, the overall 6.8 μm astronomical feature shapes could not be be well-matched in terms of either peak alignment or subpeak relative strengths.

Based on this work, we conclude that we cannot rule out NH_4^+ and CH_3OH as contributors each of at most ∼50% to the 6.8 μm band, but we emphasize that even the 50/50 combinations do not reproduce the overall feature shapes. Studies of this feature performed with higher-resolution ISO-SWS observations (e.g. Keane et al. 2001; Schutte et al. 1996) find a similar variety of structure and peak positions, confirming that it may be difficult or physically impossible to adequately explain the feature using the same set of components for all sight-lines.

5.3. The 7-8 μm Range

Because of the uncertainties due to the low resolution and low signal-to-noise of the 7-8 μm optical depth spectrum, as well as the inherent narrowness of the 7-8 μm features, we did not attempt to fit the shape of the spectral features with laboratory profiles but rather focused on detection of the 7.25 μm HCOOH, ∼7.6 μm SO_2, and 7.7 μm CH_4 features.

5.3.1. HCOOH

The 7.25 μm HCOOH band is intrinsically ∼4 times weaker than the 5.85 μm one (Bisschop et al. 2007). Based on the amount of HCOOH in the fitted spectra in Section 5.1, the expected 7.25 μm optical depths in the YSO spectra are $\lesssim 0.02$. Indeed, we do observe small features at 7.25 μm in 6 of our 16 objects. It should be noted, however, that the strength of these do not correlate with the HCOOH column densities derived from the spectral fits and the stronger 5.85 μm feature ($r = 0.06$); there are also other species with weak signatures very close to this wavelength (e.g. $HCOO^-$ and $HCONH_2$; Schutte et al. 1999). As the optical depth profiles here are neither strong nor resolved enough to conclusively distinguish among these species' signatures, these HCOOH detections must remain tentative.

5.3.2. CH_4 and SO_2

In 13 of our 16 objects, we observe a feature near 7.7 μm, where the (ν_4) C-H deformation mode of CH_4 is expected. Laboratory studies have shown that this resonance's position and width are strongly dependent on the molecular environment, becoming blue-shifted (as far as 7.64 μm) and broadened when mixed with a variety of other ices, including H_2O, CO, CH_3OH, and CO_2 (Boogert et al. 1997). In addition, there is the possibility of blending with the nearby SO_2 feature, whose 7.58 μm S-O stretching band has been shown to vary its peak position from 7.45-7.62 μm, depending on the temperature and the molecular environment (Boogert et al. 1997).

In order to disentangle absorption due to SO_2 and CH_4, we fit each YSO's 7.45-8 μm wavelength range with two Gaussian curves, allowing the peak of one (representing SO_2) to shift between 7.45-7.62 μm and constraining the other peak (CH_4) to 7.62 μm or larger. A Gaussian approximation was chosen because both the SO_2 and CH_4 profiles are too narrow, compared with the IRS resolution, to evaluate any substructure. In many cases, a single Gaussain was sufficient, indicating a single, distinct feature of either SO_2 or CH_4, depending on peak position. Of our 16 YSOs, 7 show only a 7.7 μm feature with little or no asymmetrical excess, 3 only have a distinct feature peaking within the SO_2 range, 4 show both distinct features, and 2 show a broad absorption with additional peaks within the SO_2 range (i.e. fit by overlapping Gaussians). Using the range of laboratory feature FWHMs measured by Boogert et al. (1997), we find that in 4 of the 9 objects with either distinct features or a Gaussian fit in the 7.45-7.62 μm range, the feature width is too narrow ($\Delta\lambda \lesssim 0.06$ μm) to be attributed to solid SO_2. These may be due to random noise creating an apparent peak or to CH_4 gas lines found between ~7.4-8 μm. SO_2 also has gas lines in this region, but these are very weak (Boogert et al. 1997). For the 5 remaining features, we use Equation 3.3 with a band strength A_{SO_2}=3.4×10^{-17}cm molec^{-1} (Khanna et al. 1988) to determine the SO_2 column density; for the other objects, an upper limit to $N(SO_2)$ is determined (Table 5).

Of the 13 objects with a distinct 7.7 μm CH_4 feature or Gaussian fit, 7 have FWHMs comparable to those observed in laboratory mixtures (Boogert et al. 1997), particularly in those mixtures where CH_4 and either H_2O, CH_3OH, or NH_3 exist in roughly equal abundance. The remaining 6 objects have wider features, which may be explained by variations in temperature or ice mantle composition along the line of sight. To determine the column density of CH_4 towards each YSO, we use Equation 3.3 with a band strength A_{CH_4}=7.3×10^{-18}cm molec^{-1} (pure CH_4; discussion in Boogert et al. 1997) and integrate the optical depth between 7.6-7.9 μm. Upper limit estimates for the 3 non-detections are provided by the noise in the spectrum (Table 5).

5.4. The 15.2 μm Feature

Double-peaked structure in the 15.2 μm feature, often observed in systems with an exposed source of heating and radiation (such as Class I/II objects), is associated with the dual peaks of the degenerate ν_2 bending mode in pure CO_2 ice. This structure becomes less pronounced or disappears altogether when the apolar CO_2 molecules are embedded in an H_2O-rich polar matrix (e.g. Ehrenfreund et al. 1999). Thus the presence of a double-peaked feature indicates that thermal processing has occured, segregating the CO_2 from the polar matrix. The broad shoulder on the red side of the absorption, centered around 15.4 μm, has been attributed to CO_2 interactions with other molecules, particularly CH_3OH, and the strength and shape of the shoulder depend on both temperature and relative abundances (e.g Dartois et al. 1999). Theoretical studies suggest that solid CO_2 is formed by oxidation of CO ice (e.g. Tielens & Hagen 1982; Ruffle & Herbst 2001), so the co-existence and interaction with solid CH_3OH (also formed from CO; Tielens & Charnley 1997) is not unexpected.

In the fits, made for the high-resolution spectra[2] between 14.7 and 16 μm, we include cold (10-30 K) deposits of H_2O:CO_2, pure CO_2, and an irradiated deposit of CO:H_2O, as well as warmer ($\gtrsim$100 K) mixtures of H_2O:CH_3OH:CO_2 (Table 6). The cold mixtures containing H_2O are used to estimate the contribution from nonprocessed material along the line of sight. The warmer H_2O:CH_3OH:CO_2 spectra represent ices which have been warmed and have undergone the chemical and physical changes, including segregation of the CO_2, resulting from that processing. The pure CO_2 component, though measured at 10 K, does not greatly differ in shape until sublimation at ~80 K and is here used as a measure of segregated, highly-processed ice.

Our fitting components differ from the recent work by Pontoppidan et al. (2008), which is focused almost exclusively on detailed methanol-free CO:CO_2:H_2O mixtures. Certainly these combinations can produce good fits to the CO_2 ice feature. However, in the following we will adhere to the conventional approach involving a warm CH_3OH ice component, since we find that in most cases this produces better fits to our spectra than methanol-free mixtures, and it takes into account the strong evidence of solid methanol in many protostellar environments (e.g. Pontoppidan et al. 2003; Gibb et al. 2004). It is worth noting that, since good fits are obtained by both classes of models, neither method should be thought to provide a unique solution to the ice-composition analysis.

---

[2] The low-resolution spectra are insufficient to resolve any structure which might be present.

Using a single component fit, we find that a nearly equal-parts mixture of H_2O:CH_3OH:CO_2 at temperatures of $\gtrsim$100 K provides the lowest-χ^2_ν fit to the observed YSO 15.2 μm absorption bands, in accordance with previous results for more massive protostars (e.g. Ehrenfreund et al. 1999; Gerakines et al. 1999). Where present, the dual peak positions align, and the approximate strength of the 15.4 μm shoulder is replicated. The fit improves, however, by an average of $\sim$50% of χ^2_ν, when we allow multiple components (Figure 9). The combination of these additional components reproduces the relative peak strengths, the inter-peak dip depth, and the shape of the 15.4 μm shoulder without requiring a specific single temperature.

Our multicomponent fits indicate that for our YSO sample, a smaller amount of CH_3OH ($\sim$14%) at lower temperatures is sufficient to account for the observed 15.4 μm shoulder, and equal parts H_2O, CO_2, and CH_3OH are reflected at high temperatures (higher than those identified by e.g Ehrenfreund et al. 1999), when the CO_2 has at least partly migrated out of the matrix. Laboratory mixtures at these higher temperatures that also contain the smaller fractions of CH_3OH have an asymmetrical dual peak that is not observed in the YSO spectra; mixtures with H_2O, CH_3OH, and CO_2 in a 1:1:1 ratio at lower temperatures show a stronger shoulder at 15.4 μm (relative to the main peak) as well as a nearly-single peak at 15.2 μm. While the cold-surface formation processes and expected abundances of CH_3OH are not tightly-constrained (e.g. Tielens & Whittet 1996; Keane et al. 2001, and references therein), the generally-higher abundances observed towards high-mass protostars are evidence that warmer environments may be conducive to additional CH_3OH production. This is consistent with the stronger 15.4 μm shoulders observed towards massive protostars (compared with low-mass ones; e.g. Ehrenfreund et al. 1998; Boogert et al. 2004), and the equal-parts H_2O:CH_3OH:CO_2 mixtures required to fit them. Most of our YSO fits are further improved by including the very cold ($\sim$30 K) CO:H_2O layer, representing absorption along the line of sight due to cold material, affected by the region's radiation field but too distant or too shielded from the central source to have undergone thermal heating.

Methanol-bearing ice mixtures have distinctive absorptions elsewhere in the mid-infrared spectrum, notably at 6.8 and 9.8 μm. The former feature is discussed above (Section 5.2). The latter unfortunately lies in the very bottom of the silicate absorption feature. In the mixtures that best fit the 15.2 μm ice feature, the 9.8 μm feature is either very weak or not particularly sharp. Thus it is difficult to separate possible 9.8 μm methanol ice absorption from small silicate-feature profile variation. In general, a combination of absorption from the ice mixture that best fits the 15.2 μm feature, and from interstellar silicate grains (toward

GCS 3; Kemper et al. 2004), can be made to fit the spectrum, as illustrated in Figure 10. However, this result depends sensitively on the fit of the continuum and the silicate absorption profile, which as noted above is not very well-defined for these types of environments. We found no meaningful, quantitative constraints on a putative CH_3OH ice component from the 9.8 μm feature.

The 15.2 μm features in the molecular cloud sight-lines have previously been fitted with predominantly cold, polar H_2O:CO_2 mixtures (Bergin et al. 2005; Knez et al. 2005). We find that the χ^2_ν of the fits can be matched or reduced by including components containing methanol—specifically, the cold counterparts of the H_2O:CH_3OH:CO_2 components used in our Class I/II fits described above (Figure 11). The percentage of polar ice found (∼75-80%) is comparable to that identified by Bergin et al. (2005) and Knez et al. (2005), and the abundance ratios $N(CO_2)/N(H_2O)$ from those studies are preserved.

We have calculated the total CO_2 column density (Table 5) observed along each embedded-object and molecular cloud line of sight using Equation 2. The exact band strengths of some of the laboratory mixtures used in the 15.2 μm fits are undetermined. The fitting results indicate that the vast majority of the CO_2 ice resides alongside H_2O ice, so we use a band strength of 1.5×10^{-17}cm molec^{-1}, which is appropriate for the 15.2 μm absorption from a H_2O:CO_2 1.6:1 ice (Gerakines et al. 1995). The observed optical depth spectra were integrated between 14.7-16 μm. We use the relative contributions of each fitting component to estimate the column density of solid CO_2 in each stage of thermal processing (Table 7): radiation-only (10-30 K, "cold"), some thermal heating ("warm"), and CO_2 segregation. We have also estimated the column density of solid CH_3OH embedded in CO_2 using the the CH_3OH abundance and relative contribution of each laboratory fit component (Table 5).

6. DISCUSSION

6.1. Ice Composition: Abundances With Respect to H_2O

6.1.1. CO_2 Column Density

The column densities observed in our sample of Class I/II YSOs yield $N(CO_2)/N(H_2O) \sim 0.12(\pm0.04)$ (Table 5, Figure 12), which is consistent with the values previously derived for many different lines-of-sight, averaging $N(CO_2)/N(H_2O) \sim 0.17(\pm0.03)$ (Gerakines et al. 1999; Nummelin et al. 2001; Gibb et al. 2004; Knez et al. 2005; Alexander et al. 2003), but significantly lower than the value of $N(CO_2)/N(H_2O) \sim 0.3$, with large scatter, reported by Boogert et al. (2004) and Pontoppidan et al. (2008). Our study is unique in the sense that we use the band strength A_{CO_2} of an H_2O:CO_2 mixture. If we instead use the band strength for pure CO_2, we find $N(CO_2)/N(H_2O) \sim 0.16(\pm 0.04)$, nearly equivalent to the results of the majority of previous studies, which include high- and low-mass YSOs, background field stars sampling molecular clouds, and galactic center sight-lines sampling diffuse interstellar material and molecular clouds.

The dashed line in Figure 4 identifies the locus of compositions with $CO_2/H_2O = 0.12$, which are clearly underrepresented in the heated samples from the Leiden University database. Good profile fits can only be achieved by combining ice mixtures, and this gap in composition-space may explain some of the difficulty experienced in fitting 6 μm features. Further laboratory exploration of the water-rich mixtures around the observed ratio with CO_2 may help to improve constraints on the column density of H_2O ice based on the 6 μm feature.

6.1.2. Evolutionary Trends in CO_2

When considering the Class I/II sample in conjunction with the Class 0 objects, we find $N(H_2O)$ to be well-correlated ($N(CO_2)$ less so) with the spectral index α, where more embedded sources (higher α) show higher column densities, as is expected (Figure 13; top 2 panels). The ratio $N(CO_2)/N(H_2O)$ increases as the objects evolve towards lower α-values (Figure 13; bottom panel).

The sublimation temperature of solid H_2O is ~40 K higher than that of pure CO_2 ice (Gerakines et al. 1995). Thus with increased exposure to thermal radiation, $N(CO_2)/N(H_2O)$ is expected to go down, seemingly contradicting our observations. Although CO_2 molecules embedded in a polar matrix may become "trapped" and able to survive to temperatures nearing the sublimation limit of H_2O, the thermal destruction of H_2O before CO_2 is unlikely.

An explanation of the high column density of CO_2 in more exposed environments may be found in the formation of additional CO_2 in Class I/II objects. Photodissociation of H_2O leads to the production of radicals (e.g. OH) which can react to form CO_2 on the grain surface (e.g. $CO+OH \rightarrow CO_2$; Allamandola et al. 1988). Some other reaction pathways to form CO_2 in molecular clouds and star-forming regions have activation barriers which become less obstructive in warmer, more exposed environments (e.g Ruffle & Herbst 2001; van Dishoeck & Blake 1998). Indeed, in UV-irradiated H_2O:CH_3OH:CO_2 laboratory samples, CO_2 eventually reaches a constant abundance level due to an equilibrium between destruction and formation (Ehrenfreund et al. 1999), while the abundance of H_2O further decreases due to photodissociation.

The values measured towards the background stars Elias 16, Elias 13, and CK 2 cannot be extrapolated from this trend. The $N(CO_2)/N(H_2O)$ ratios for these lines-of-sight (Table 8) are not lower than the ratios observed towards the YSOs. This discrepancy may be due to the fact that the interstellar lines-of-sight probe a variety of environments and compositional structure, while protostellar sight-lines are dominated by the circumstellar material. Possibly, the lower temperatures in interstellar regions stifle CO_2 formation mechanisms with activation barriers, while areas of increased density favor H_2O production.

6.1.3. HCOOH

Apart from one outlier at $N(H_2O) \sim 1.1{\times}10^{19}\mathrm{cm}^{-2}$ (L1551 IRS 5), the column densities of HCOOH and H_2O are strongly related ($r = 0.61$, Figure 14). This supports laboratory experiments demonstrating that the most likely formation environments of solid HCOOH are those that also produce H_2O ice, through either radiative processing or cold surface reactions (Bisschop et al. 2007). We find $N(HCOOH)/N(H_2O) \sim$ 0-2%, with an average of 0.6%, well within the $\lesssim$5% abundance ratio observed in lines-of-sight towards massive and low-mass protostars (Bisschop et al. 2007; Boogert et al. 2008).

6.1.4. CH_3OH

The observed $N(CH_3OH)/N(H_2O)$ ratios in our sample do not show a clear trend (Figure 14). It is known that the $N(CH_3OH)/N(H_2O)$ abundance varies greatly from source to source (e.g Boogert & Ehrenfreund 2004), and it may be better to analyze the CH_3OH abundance with respect to CO_2.

CH_3OH can be detected in the spectrum in three places. When it is intermixed with CO_2, a shoulder at 15.4 μm due to CH_3OH can be observed in the 15.2 μm feature; and CH_3OH also shows 6.8 and 9.8 μm bands (the latter is blended in the 9.7 μm silicate complex). In Figure 15 we show the ratio of the optical depth at 15.4 μm (vertical axis) and 6.8 μm (horizontal axis), both with respect to the optical depth at 15.2 μm. Filled circles represent the astronomical measurements, while the plus signs indicate the ratios measured in the laboratory spectra. The laboratory spectra show a correlation between the two features, whose exact position depends on the temperature. The 15.4/15.2 μm τ ratios observed in the astronomical data are within the range measured in the laboratory, but the corresponding 6.8 μm optical depths are significantly greater than the laboratory values. This could be understood if only a small fraction of the CH_3OH along the line of sight is embedded in a CO_2

matrix or if there are significant contributions to the 6.8 μm feature from other components.

Using the laboratory fits to the 15.2 μm complex in the high spectral resolution data, we estimate the column density of solid CH_3OH intermixed with CO_2 as 30-56% with respect to CO_2, corresponding to $N(CH_3OH)_{CO_2}/N(H_2O) \sim$ 2-9% (Table 5). Assuming that $\lesssim$50% of the 6.8 μm feature is due to to CH_3OH (Section 5.2.3), we estimate $N(CH_3OH)_{\rm total}/N(H_2O)$ $\lesssim$ 5-17%. There are two outlying values, for IRAS 04108+2803A and IRAS 04181+2654B, at 32 and 28%. Although we do not place high confidence in these as absolute values because of the 6.8 μm uncertainties, they are consistent with the detection of solid CH_3OH with abundances (relative to H_2O) in this range up to ∼25% towards low-mass YSOs (as well as the overall scatter in abundance; Pontoppidan et al. 2003; Boogert et al. 2008). Thus our data support the presence of a significant CO_2-poor H_2O:CH_3OH ice component.

6.1.5. CH_4

We observe a range of $N(CH_4)/N(H_2O)$ ratios from ∼0.3 to 8% in our sample (Figure 16), with an average of 2.6% and a single outlier (IRAS 04154+2823) at 23% . Our measurements largely overlap with the ratios of ∼0.5-4% reported in the literature (e.g. Boogert et al. 1996; Gibb et al. 2004), though ratios up to 13% are reported by Öberg et al. (2008). The higher values in our sample (>4%, dashed line in Figure 16) may be partially ascribed to additional absorptions unresolvable at the SL-module resolution, such as gas-phase CH_4 lines (Boogert et al. 1997), or to matrix-dependent variations in band strength. Hudgins et al. (1993) found that the band strength for the 7.7 μm CH_4 feature may vary by as much as a factor of 2.8 between H_2O-rich and CO-rich matrices. We use the value for pure CH_4, which lies approximately midway between the two extremes.

Laboratory studies of solid CH_4 indicate that it can be formed by a variety of processes—including UV photolysis of CH_3OH ices (Allamandola et al. 1988) and grain-surface hydrogenation of carbon (Tielens & Hagen 1982)—and that the resulting absorption profile has characteristics unique to its formation pathway and embedding matrix (Boogert et al. 1997). Unfortunately, the low signal-to-noise of the CH_4 detections, and the low spectral resolution, prevent a detailed analysis of the spectral profiles; however, the broad range of peak positions and widths implies that the CH_4 embedding matrices vary across the sample.

6.2. Segregation of CO_2 Ice

In the colder parts ($\lesssim$20 K) of a star-forming region, well-removed from the hot cores and embedded protostars or buried in dense clumps, apolar CO_2 ice is formed embedded in a polar H_2O matrix (e.g. Boogert & Ehrenfreund 2004). The 15.2 μm CO_2 resonance will appear to be broad and single-peaked. As these ices are heated, as for instance happens in the circumstellar environments of YSOs, the CO_2 can migrate out of the polar matrix and aggregate, either as a surface layer or in bulk apolar clumps within the matrix (e.g. Sandford & Allamandola 1990; Ehrenfreund et al. 1999). The spectral appearance of the CO_2 resonance changes, and a double-peaked structure, with peaks at 15.1 and 15.25 μm, becomes apparent rather rapidly (Figure 17). The migration process also destabilizes the CO_2:CH_3OH interactions and reduces the 15.4 μm shoulder. Due to the apparent spectral difference between segregated CO_2 ice and CO_2 ice embedded in an H_2O:CH_3OH matrix, it is possible to determine the relative mass contained in both of these phases.

In Figure 18, we show the variation in the CO_2 15.2 μm absorption feature in our sample, along with laboratory spectra of CO_2 fully embedded in the matrix (top; 10 K) and fully segregated CO_2 (bottom; 130 K). The dashed lines indicate the positions of the double-peaked segregated CO_2 and the shoulder at 15.4 μm due to embedded CO_2 interacting with CH_3OH. We show only the Class I/II objects for which high resolution spectra are available, as the double-peaked structure is not resolved in the low resolution spectra. Several of the spectra clearly show the double-peaked structure, while all deviate from the smooth, unprocesed Taurus cloud profiles as published by Whittet et al. (2007), Bergin et al. (2005), and Knez et al. (2005). Indeed, from the multi-component fits described in Section 5.4, we find evidence in all of our low-mass YSO spectra for moderate-temperature thermal processing ($\lesssim$100 K; CO_2 warmed but not segregated), in agreement with Boogert et al. (2004) but in contrast with Nummelin et al. (2001). However, unlike Boogert et al. (2004), we also find evidence for high-temperature processing—5 of the 9 objects (IRAS 04016+2610, IRAS 04239+2436, IRAS 04365+2535, DG Tau B, and IC 2087 IR) have 15.2 μm profiles entirely dominated by warmed ices in which a significant fraction ($\sim$20-40%) of the CO_2 has segregated from the polar formation matrix.

From the multi-component fits, we can derive the mass distribution of CO_2 ice over the *phases* (cold, warm, segregated). The phase transitions correspond to laboratory temperatures, which in turn translate to (lower) astrophysical temperatures. The onset of CO_2 segregation occurs at a temperature near 105 K in the laboratory (Figure 17), which corresponds to an astrophysical temperature of $\sim$65 K (e.g. Boogert et al. 2000). The CO_2 evaporation temperature depends on the relative abundance of other species, particularly H_2O, but the mixtures with the most physically likely abundances (i.e. $CO_2/H_2O < 1$)

show an average sublimation temperature of ∼150 K, or 80 K in astrophysical environments. Thus, the *segregated* column densities of Table 7 represent CO_2 ice at circumstellar radii where the ice temperature is between 65 and 80 K, and the *cold+warm* column densities indicate ice farther from the central source (i.e. where $T < 65$ K). The inner boundary of the segregated CO_2 ice zone is defined by the evaporation temperature at ∼80 K. The low-mass protostellar envelope models produced by Furlan et al. (2008) for nearly all the stars in our sample indicate these approximate temperature ranges in the densest inner regions ($R \lesssim 100$ AU); however, detailed physical structure models that also include the appropriate ice opacities are needed to further constrain the location and processing levels of the ices.

In Figure 19 we show the correlation of thermal processing levels with the SED spectral index (indicative of the line-of-sight dust column). While there is a large amount of scatter in these plots, the overall fraction of cold CO_2 ice increases (and the warm fraction decreases) for more deeply embedded objects, while the segregated fraction does not show a clear trend with total dust opacity.

6.2.1. Segregation of CO_2 Ice in Molecular Clouds and W3(OH)

All three interstellar cloud sight-lines show single-peaked 15.2 μm profiles with very little substructure; CK 2 and Elias 16 are remarkably similar in shape (Figure 11), despite indications that ice mantles in Serpens may be fundamentally different from those in Taurus (e.g Eiroa & Hodapp 1989; Whittet et al. 2007). These results give support for the cold grain origin of at least some of the CH_3OH observed towards protostars; the presence of the unidentified 6.8 μm band in background star sight-lines (in particular CK 2 and Elias 16; Knez et al. 2005) is consistent with the assignment of CH_3OH as a carrier.

Interestingly, the spectrum of W3(OH), which has the reddest SED of our entire sample, shows a clearly double-peaked CO_2 feature, indicating pure CO_2 along the line of sight, which could have been formed by thermal segregation (Figure 20). The segregation fraction is ∼26%, comparable to the Class I/II average of ∼30%. Given the difference in segregation with the pure molecular cloud lines of sight, the most likely explanation is that this line of sight samples not only the cold foreground W3 cloud but also the warmer, thermally-processed CO_2 ices around the massive protostars in the W3(OH) region. The strong similarity of the 15.2 μm absorption profile towards W3(OH) to those of the low-mass Taurus objects is curious, as the line of sight toward W3(OH) is highly diverse, containing an ultra-compact HII region, strong outflows, and H_2O/OH maser emissions (Turner & Welch 1984; Alcolea et al. 1993; Argon et al. 2003). Future spectroscopic observations with higher angular resolution will resolve the spatial structure and provide useful information on the complexity of the early stages of CO_2 heating in embedded objects.

7. CONCLUSIONS

We have analyzed the mid-infrared molecular ice features in 16 Class I/II low-mass YSOs using Spitzer IRS observations. Using detailed comparisons to laboratory ice analog spectra, we find the ice mantle compositions to be dominated by H_2O and CO_2 ice but with significant abundances of additional species such as CH_3OH, H_2CO, HCOOH, NH_3, CH_4, and SO_2 ($\lesssim$10% each).

Detailed spectral fits to the 6 μm feature reveal that $\gtrsim$80% of the band can be attributed to H_2O, with additional absorptions near 5.85 μm identified as HCOOH and H_2CO. Some of the observed spectra have a broader 6 μm peak that can be well-fit by H_2O:NH_3 ices, providing evidence for the presence of solid NH_3. On the long-wavelength wing of the 6 μm feature, small absorption remnants are observed, varying in strength, shape, and peak position among the sources. We show that these are highly unlikely to be the result of PAH absorption, due to the absence of other expected PAH features at 7.5-9 and 11-14 μm.

We have examined the unidentified 6.8 μm feature and discussed its assignment to solid CH_3OH and NH_4^+, the two most common candidates. While no high-quality spectral fits could be achieved using these two components, we find that on average the observed YSO features could be approximately fit by equal contributions from NH_4^+ and from a $CH_3OH/H_2O\sim0.1$ mixture, with varying amounts of nearly-pure CH_3OH intermixed. However, we find a wide variety of feature shapes in our sample, indicating that the interstellar component(s) producing this band vary greatly from object to object, and a single simple carrier or set of carriers may be inadequate to explain the feature.

In the 7-8 μm range, we are able to isolate and identify features attributed to CH_4, SO_2, and (tentatively) HCOOH ices. The high CH_4 ice abundances derived from these, along with the variety of feature shapes and peak positions within the sample, suggest variations in line-of-sight molecular environment or possible absorption contamination by unresolvable gas-phase CH_4 lines. The solid SO_2 and CH_4 band profiles are very sensitive to molecular environment and temperature, and additional high-resolution studies of this wavelength range will yield further information on molecular ice interactions and abundance structures along the line of sight.

The 15.2 μm solid CO_2 bending mode feature is well-reproduced by multi-component laboratory fits comprising ice analogs (H_2O, CH_3OH, CO, CO_2) in various stages of radiative and thermal processing. Using the relative contribution of the components to each high-resolution feature profile, we find that all of the YSO ice environments have undergone at least some thermal heating, and 5 of the 9 have profiles entirely dominated by processed ices in which a significant fraction ($\sim$20-40%) of the CO_2 has segregated from the polar formation matrix.

The molecular ice abundance ratios, particularly $N(CO_2)/N(H_2O)$, are consistent with the values observed in a wide variety of sight-lines, but within the sample, we observe a negative correlation between this ratio and the mid-infrared SED spectral index. This evidence describes a more complicated polar CO_2 environment than indicated by previous studies. Comparison of the SED spectral index with the ice temperatures derived from the 15.2 μm fits confirms the presence of cold ices in more deeply embedded objects and warmer, annealed ices in more evolved ones.

Comparison with molecular cloud sight-lines show that our fits are consistent with a scenario in which H_2O-rich grain mantles with CO_2 and CH_3OH relative abundances of $\sim$20 and $\lesssim$10%, respectively, as well as traces of other species, form in the cold molecular clouds and are subsequently heated by young protostars. This thermal processing sublimates the most volatile species while inducing molecular interactions and migrations that become spectroscopically detectable. The wide range of both molecular abundances and thermal processing levels observed within our sample indicates that young stars have a strong effect on their surrounding environments.

We are grateful to Edwin Bergin and Claudia Knez for providing us with the field star spectra, to Melissa McClure for assistance with data reduction issues, and to Adwin Boogert for stimulating discussion. Extensive use was made of Leiden University's Sackler Laboratory ice analog databases and of the NASA ADS Abstract Service. This work is based on observations made with the Spitzer Space Telescope, which is operated by the Jet Propulsion Laboratory, California Institute of Technology under NASA contract 1407. Support for this work was provided by NASA through Contract Number 1257184 issued by JPL/Caltech. E.F. acknowledges support from a NASA Postdoctoral Program Fellowship.

REFERENCES

Alcolea, J., Menten, K. M., Moran, J. M., & Reid, M. J. 1993, in Lecture Notes in Physics, Berlin Springer Verlag, Vol. 412, Astrophysical Masers, ed. A. W. Clegg & G. E. Nedoluha, 225–228

Alexander, R. D., Casali, M. M., André, P., Persi, P., & Eiroa, C. 2003, A&A, 401, 613

Allamandola, L. J., Sandford, S. A., & Valero, G. J. 1988, Icarus, 76, 225

Argon, A. L., Reid, M. J., & Menten, K. M. 2003, ApJ, 593, 925

Bergin, E. A., Melnick, G. J., Gerakines, P. A., Neufeld, D. A., & Whittet, D. C. B. 2005, ApJ, 627, L33

Bertout, C., Robichon, N., & Arenou, F. 1999, A&A, 352, 574

Bisschop, S. E., Fuchs, G. W., Boogert, A. C. A., van Dishoeck, E. F., & Linnartz, H. 2007, A&A, 470, 749

Boogert, A. C. A. & Ehrenfreund, P. 2004, in Astronomical Society of the Pacific Conference Series, Vol. 309, Astrophysics of Dust, ed. A. N. Witt, G. C. Clayton, & B. T. Draine, 547–+

Boogert, A. C. A., Ehrenfreund, P., Gerakines, P. A., et al. 2000, A&A, 353, 349

Boogert, A. C. A., Pontoppidan, K. M., Knez, C., et al. 2008, ApJ, 678, 985

Boogert, A. C. A., Pontoppidan, K. M., Lahuis, F., et al. 2004, ApJS, 154, 359

Boogert, A. C. A., Schutte, W. A., Helmich, F. P., Tielens, A. G. G. M., & Wooden, D. H. 1997, A&A, 317, 929

Boogert, A. C. A., Schutte, W. A., Tielens, A. G. G. M., et al. 1996, A&A, 315, L377

Bottinelli, S., Ceccarelli, C., Lefloch, B., et al. 2004, ApJ, 615, 354

Cazaux, S., Tielens, A. G. G. M., Ceccarelli, C., et al. 2003, ApJ, 593, L51

Chan, K. W., Roellig, T. L., Onaka, T., et al. 2000, in ESA Special Publication, Vol. 456, ISO Beyond the Peaks: The 2nd ISO Workshop on Analytical Spectroscopy, ed. A. Salama, M. F. Kessler, K. Leech, & B. Schulz, 59–+

Chiar, J. E., Adamson, A. J., Kerr, T. H., & Whittet, D. C. B. 1995, ApJ, 455, 234

Chiar, J. E., Ennico, K., Pendleton, Y. J., et al. 2007, ApJ, 666, L73

Dartois, E., Demyk, K., d'Hendecourt, L., & Ehrenfreund, P. 1999, A&A, 351, 1066

Ehrenfreund, P., Boogert, A. C. A., Gerakines, P. A., et al. 1996, A&A, 315, L341

Ehrenfreund, P., Dartois, E., Demyk, K., & D'Hendecourt, L. 1998, A&A, 339, L17

Ehrenfreund, P., Kerkhof, O., Schutte, W. A., et al. 1999, A&A, 350, 240

Eiroa, C. & Hodapp, K.-W. 1989, A&A, 210, 345

Forrest, W. J., Sargent, B., Furlan, E., et al. 2004, ApJS, 154, 443

Furlan, E., Hartmann, L., Calvet, N., et al. 2006, ApJS, 165, 568

Furlan, E., McClure, M., Calvet, N., et al. 2008, ApJS, 176, 184

Gerakines, P. A., Schutte, W. A., & Ehrenfreund, P. 1996, A&A, 312, 289

Gerakines, P. A., Schutte, W. A., Greenberg, J. M., & van Dishoeck, E. F. 1995, A&A, 296, 810

Gerakines, P. A., Whittet, D. C. B., Ehrenfreund, P., et al. 1999, ApJ, 522, 357

Gibb, E. L., Whittet, D. C. B., Boogert, A. C. A., & Tielens, A. G. G. M. 2004, ApJS, 151, 35

Gibb, E. L., Whittet, D. C. B., Schutte, W. A., et al. 2000, ApJ, 536, 347

Gillett, F. C., Jones, T. W., Merrill, K. M., & Stein, W. A. 1975, A&A, 45, 77

Gomez, M., Hartmann, L., Kenyon, S. J., & Hewett, R. 1993, AJ, 105, 1927

Grim, R. J. A., Baas, F., Greenberg, J. M., Geballe, T. R., & Schutte, W. 1991, A&A, 243, 473

Grim, R. J. A., Greenberg, J. M., Schutte, W. A., & Schmitt, B. 1989, ApJ, 341, L87

Hagen, W., Tielens, A. G. G. M., & Greenberg, J. M. 1981, Chem. Phys., 56, 367

Higdon, S. J. U., Devost, D., Higdon, J. L., et al. 2004, PASP, 116, 975

Hony, S., Van Kerckhoven, C., Peeters, E., et al. 2001, A&A, 370, 1030

Houck, J. R., Roellig, T. L., van Cleve, J., et al. 2004, ApJS, 154, 18

Hudgins, D. M., Sandford, S. A., Allamandola, L. J., & Tielens, A. G. G. M. 1993, ApJS, 86, 713

Indebetouw, R., Mathis, J. S., Babler, B. L., et al. 2005, ApJ, 619, 931

Keane, J. 1997, Master's thesis, Leiden University

Keane, J. 2001, PhD thesis, Rijks Universiteit Groningen

Keane, J. V., Tielens, A. G. G. M., Boogert, A. C. A., Schutte, W. A., & Whittet, D. C. B. 2001, A&A, 376, 254

Kemper, F., Vriend, W. J., & Tielens, A. G. G. M. 2004, ApJ, 609, 826

Kenyon, S. J. & Hartmann, L. 1995, ApJS, 101, 117

Khanna, R. K., Zhao, G., Ospina, M. J., & Pearl, J. C. 1988, Spectrochimica Acta, 44, 581

Knez, C., Boogert, A. C. A., Pontoppidan, K. M., et al. 2005, ApJ, 635, L145

Kouchi, A. & Kuroda, T. 1990, Nature, 344, 134

Lacy, J. H., Faraji, H., Sandford, S. A., & Allamandola, L. J. 1998, ApJ, 501, L105+

Lada, C. J. 1987, in IAU Symposium, Vol. 115, Star Forming Regions, ed. M. Peimbert & J. Jugaku, 1–17

Maldoni, M. M., Smith, R. G., Robinson, G., & Rookyard, V. L. 1998, MNRAS, 298, 251

Maréchal, Y. 1987, J. Chem. Phys., 87, 6344

Mathis, J. S. 1990, ARA&A, 28, 37

Moore, M. H. & Hudson, R. L. 1992, ApJ, 401, 353

Myers, P. C., Linke, R. A., & Benson, P. J. 1983, ApJ, 264, 517

Nummelin, A., Whittet, D. C. B., Gibb, E. L., Gerakines, P. A., & Chiar, J. E. 2001, ApJ, 558, 185

Öberg, K. I., Boogert, A. C. A., Pontoppidan, K. M., et al. 2008, ApJ, 678, 1032

Öberg, K. I., Fraser, H. J., Boogert, A. C. A., et al. 2007, A&A, 462, 1187

Palumbo, M. E. & Baratta, G. A. 2000, A&A, 361, 298

Pontoppidan, K. M., Boogert, A. C. A., Fraser, H. J., et al. 2008, ApJ, 678, 1005

Pontoppidan, K. M., Dartois, E., van Dishoeck, E. F., Thi, W.-F., & d'Hendecourt, L. 2003, A&A, 404, L17

Pontoppidan, K. M., Dullemond, C. P., van Dishoeck, E. F., et al. 2005, ApJ, 622, 463

Puetter, R. C., Russell, R. W., Willner, S. P., & Soifer, B. T. 1979, ApJ, 228, 118

Remijan, A., Shiao, Y.-S., Friedel, D. N., Meier, D. S., & Snyder, L. E. 2004, ApJ, 617, 384

Rieke, G. H. & Lebofsky, M. J. 1985, ApJ, 288, 618

Ruffle, D. P. & Herbst, E. 2001, MNRAS, 324, 1054

Sandford, S. A. & Allamandola, L. J. 1990, ApJ, 355, 357

Sandford, S. A. & Allamandola, L. J. 1993, ApJ, 417, 815

Schutte, W. A., Allamandola, L. J., & Sandford, S. A. 1993, Icarus, 104, 118

Schutte, W. A., Boogert, A. C. A., Tielens, A. G. G. M., et al. 1999, A&A, 343, 966

Schutte, W. A. & Khanna, R. K. 2003, A&A, 398, 1049

Schutte, W. A., Tielens, A. G. G. M., Whittet, D. C. B., et al. 1996, A&A, 315, L333

Tielens, A. G. G. M. & Allamandola, L. J. 1987, in Astrophysics and Space Science Library, Vol. 134, Interstellar Processes, ed. D. J. Hollenbach & H. A. Thronson, Jr., 397–469

Tielens, A. G. G. M., Allamandola, L. J., Bregman, J., et al. 1984, ApJ, 287, 697

Tielens, A. G. G. M. & Charnley, S. B. 1997, Origins of Life and Evolution of the Biosphere, 27, 23

Tielens, A. G. G. M. & Hagen, W. 1982, A&A, 114, 245

Tielens, A. G. G. M. & Whittet, D. C. B. 1996, in IAU Symposium, Vol. 178, Molecules in Astrophysics: Probes & Processes, ed. E. F. van Dishoeck, 45–+

Turner, J. L. & Welch, W. J. 1984, ApJ, 287, L81

van Broekhuizen, F. A., Groot, I. M. N., Fraser, H. J., van Dishoeck, E. F., & Schlemmer, S. 2006, A&A, 451, 723

van Dishoeck, E. F. 2003, in SFChem 2002: Chemistry as a Diagnostic of Star Formation, proceedings of a conference held August 21-23, 2002 at University of Waterloo, Waterloo, Ontario, Canada N2L 3G1. Edited by Charles L. Curry and Michel Fich. NRC Press, Ottawa, Canada, 2003, p. 201., ed. C. L. Curry & M. Fich, 201–+

van Dishoeck, E. F. 2006, Proceedings of the National Academy of Science, 103, 12249 van Dishoeck, E. F. & Blake, G. A. 1998, ARA&A, 36, 317

van Dishoeck, E. F., Helmich, F. P., de Graauw, T., et al. 1996, A&A, 315, L349

Watson, D. M., Kemper, F., Calvet, N., et al. 2004, ApJS, 154, 391

Werner, M. W., Roellig, T. L., Low, F. J., et al. 2004, ApJS, 154, 1

White, R. J. & Ghez, A. M. 2001, ApJ, 556, 265

Whittet, D. C. B., Bode, M. F., Longmore, A. J., et al. 1988, MNRAS, 233, 321

Whittet, D. C. B., Boogert, A. C. A., Gerakines, P. A., et al. 1997, ApJ, 490, 729

Whittet, D. C. B., Shenoy, S. S., Bergin, E. A., et al. 2007, ApJ, 655, 332

Willner, S. P., Gillett, F. C., Herter, T. L., et al. 1982, ApJ, 253, 174

This preprint was prepared with the AAS LATEX macros v5.2.

Table 1. Overview of the Spitzer IRS observations of our sample of Class I/II objects. The first column gives the object name, and the second to fourth columns give the observations' AOR key, date, and IRS modules/mode used (SL: short-low, SH: short-high, LL: long-low, LH: long-high).

Object	AOR	Obs. Date (2004)	IRS Modules/Mode
IRAS 04016+2610	3528960	2/07	SL,SH,LH Map
IRAS 04108+2803A	3539712	2/06	SL,LL Stare
IRAS 04108+2803B	3529472	2/06	SL,SH,LH Map
IRAS 04154+2823	3534336	3/03	SL,LL Map
IRAS 04169+2702	3534848	3/04	SL,LL Map
IRAS 04181+2654A	3546112	2/29	SL,LL Stare
IRAS 04181+2654B	3545856	2/07	SL,LL Stare
IRAS 04239+2436	3530752	2/08	SL,SH,LH Map
IRAS 04295+2251	3537408	2/27	SL,LL Map
IRAS 04361+2547	3533056	2/29	SL,SH,LH Map
IRAS 04365+2535	3533312	2/27	SL,SH,LH Map
IRAS 04381+2540	3538944	2/27	SL,LL Map
DG Tau B	3540992	2/08	SL,SH,LH Stare
HL Tau	3531776	3/04	SL,SH,LH Map
IC 2087 IR	3533312	2/27	SL,SH,LH Map
L1551 IRS 5	3531776	3/04	SL,SH,LH Map

Table 2. Absorption features identified in our YSO spectra.

Wavelength (μm)	Carrier(s)	Mode	A (10^{-17}cm molec^{-1})	Reference
Ice Features				
5.81	H_2CO	C=O stretching	0.96	1
5.85	HCOOH	C=O stretching	6.7	2
6.0	H_2O	H-O-H bending	1.2-1.3[a]	3
6.8	CH_3OH?, NH_4^+?, organics	O-H bending, C-H deforming	···	
7.58	SO_2	S-O stretching	3.4	4
7.7	CH_4	C-H deforming	0.73	4
15.2	CO_2	O-C-O bending	1.5[b]	3
Other Features				
9.7	Silicates	Si-O stretching	···	
14.97	CO_2	gas-phase ν_2 bend	···	5
18-20	Silicates	O-Si-O bending	···	

[a] A depends on temperature; range represents 10-120K

[b] A for H_2O:CO_2 mix, see Section 3.3

References. — (1) Schutte et al. (1993), (2) Maréchal (1987), (3) Gerakines et al. (1995), (4) Boogert et al. (1997), (5) van Dishoeck et al. (1996)

Table 3. Characteristics of our sample of Taurus Class I/II objects. The first column gives the object name, the second and third columns give the 6.0 μm and 15.2 μm peak optical depths, and the fourth column gives the SED spectral index α (7-30 μm; Equation 3).

Object	$\tau_{6.0\mu m}$	$\tau_{15.2\mu m}$	SED α
IRAS 04016+2610	0.38(±0.01)	0.73(±0.01)	0.43(±0.02)
IRAS 04108+2803A	0.19(±0.01)	0.19(±0.01)	0.29(±0.10)
IRAS 04108+2803B	0.26(±0.01)	0.43(±0.01)	0.21(±0.07)
IRAS 04154+2823	0.08(±0.01)	0.16(±0.01)	-0.35(±0.04)
IRAS 04169+2702	0.25(±0.01)	0.31(±0.01)	0.98(±0.02)
IRAS 04181+2654A	0.2(±0.01)	0.3(±0.01)	0.08(±0.02)
IRAS 04181+2654B	0.32(±0.03)	0.44(±0.01)	0.51(±0.03)
IRAS 04239+2436	0.25(±0.01)	0.44(±0.01)	0.41(±0.05)
IRAS 04295+2251	0.2(±0.02)	0.18(±0.01)	0.47(±0.02)
IRAS 04361+2547	0.45(±0.01)	0.27(±0.03)	2.22(±0.02)
IRAS 04365+2535	0.33(±0.01)	0.63(±0.01)	0.54(±0.04)
IRAS 04381+2540	0.44(±0.01)	0.62(±0.01)	0.61(±0.03)
DG Tau B	0.34(±0.04)	0.3(±0.01)	0.38(±0.07)
HL Tau	0.12(±0.01)	0.12(±0.01)	0.34(±0.02)
IC 2087 IR	0.14(±0.01)	0.33(±0.01)	-0.89±0.01)
L1551 IRS 5	0.54(±0.01)	0.58(±0.03)	1.41(±0.02)

Table 4. Laboratory spectra used in 6 μm fits.

Composition	Temperature (K)	Radiation[a]
Pure H_2O	10	···
Pure H_2O	30	···
Pure H_2O	50	···
Pure H_2O	120	···
Pure H_2CO	10	···
Pure HCOOH	10	···
H_2O:CH_4[b] 1:0.33	50	1 hr
H_2O:NH_3 1:0.2	10	1 hr

[a] The equivalent of 10^{15}cm^{-2}s^{-1} photons ($E_\gamma > 6$ eV) for the noted length of time

[b] CH_4 does not have a resonance at 6μm, but its presence in a water ice matrix affects the shape of the feature.

References. — All spectra from Leiden University's Sackler Laboratory ice analog databases.

Table 5. Derived solid-state molecular abundances in our YSO sample. The first column gives the object name, and the second through eighth columns give the column densities of H_2O, CO_2, H_2CO, HCOOH, NH_3, SO_2, CH_4, and CH_3OH.

Object	$N(H_2O)$[a] $10^{18}\mathrm{cm}^{-2}$	$N(CO_2)$[b] % H_2O	$N(H_2CO)$ % H_2O	$N(\mathrm{HCOOH})$[c] % H_2O	$N(NH_3)$ % H_2O	$N(SO_2)$ % H_2O	$N(CH_4)$ % H_2O	$N(CH_3OH)$[d] % H_2O
IRAS 04016+2610	5.91 ± 0.2	17.4 ± 1.4	1.9	1.8	<12.1	<0.1	0.4 ± 0.4	8.3 ± 1.4
IRAS 04108+2803A	2.90 ± 0.3	9.5 ± 2.4	0.3	0.6	<9.0	1.7 ± 1.1	8.0 ± 2.6	···
IRAS 04108+2803B	4.44 ± 0.2	11.1 ± 1.5	2.2	0.8	<9.0	<0.7[e]	5.6 ± 1.2	6.3 ± 1.5
IRAS 04154+2823	1.07 ± 0.2	19.3 ± 7.9	0.1	0.0	<28.4	<0.5	23.2 ± 9.1	···
IRAS 04169+2702	4.33 ± 0.2	10.1 ± 1.5	2.4	1.0	<9.0	<0.5[e]	3.9 ± 1.2	···
IRAS 04181+2654A	3.63 ± 0.2	11.4 ± 1.8	3.6	0.2	<9.0	<0.1[e]	3.1 ± 1.4	···
IRAS 04181+2654B	4.18 ± 0.4	15.6 ± 2.3	7.1	0.7	<25.6	<0.3	4.5 ± 2.0	···
IRAS 04239+2436	4.44 ± 0.2	12.6 ± 1.5	2.4	0.0	<12.5	0.6 ± 0.2	<0.5	3.8 ± 1.5
IRAS 04295+2251	2.82 ± 0.3	9.4 ± 2.3	1.7	0.4	<15.3	<1.0[e]	2.4 ± 1.8	···
IRAS 04361+2547	7.38 ± 0.3	4.9 ± 1.5	0.0	0.9	<9.0	<0.1	4.3 ± 0.7	1.7 ± 1.5
IRAS 04365+2535	5.31 ± 0.2	15.2 ± 1.6	1.8	0.5	<13.0	<0.1	0.8 ± 0.7	8.5 ± 1.6
IRAS 04381+2540	7.92 ± 0.2	11.8 ± 0.8	0.8	0.5	<9.2	0.2 ± 0.1	0.3 ± 0.3	···
DGTauB	5.65 ± 0.6	7.5 ± 1.5	0.0	0.5	<17.7	1.2 ± 0.6	<0.4	3.5 ± 1.5
HLTau	1.91 ± 0.2	7.3 ± 2.8	5.9	0.7	<11.0	1.0 ± 0.5	<1.2	4.0 ± 2.8
IC2087IR	2.13 ± 0.2	19.5 ± 4.5	0.8	0.1	<26.7	<0.2	1.8 ± 2.2	8.7 ± 4.5
L1551IRS5	10.90 ± 0.2	8.0 ± 1.3	0.0	0.0	<9.0	<0.0	1.7 ± 0.4	3.2 ± 1.3

Note. — $N(H_2CO)$ and $N(\mathrm{HCOOH})$ have typical absolute uncertainties of ~10%.

[a] Uncertainties listed are statistical, and derived from the residual differences between the data and our models. There are potential systematic errors as well, as described in Section 5.1.1.

[b] Using band strength of H_2O:CO_2 mixture; see Section 6.1.

[c] Based on 5.8 μm feature alone.

[d] $N(CH_3OH)$ intermixed with CO_2, from high-resolution 15.2 μm feature fits.

[e] A feature was detected in the SO_2 wavelength range but with an overly-narrow width; value given is an upper limit.

Table 6. Laboratory spectra used in 15 μm fits.

Composition	Temperature (K)	Radiation[a]	Reference
H_2O:CH_3OH:CO_2 0.9:0.3:1	98	···	1
H_2O:CH_3OH:CO_2 1:1:1	130	···	1
CO:H_2O 10:1	30	1 hr	2
H_2O:CO_2 10:1	10	···	3
Pure CO_2	10	···	3

[a] The equivalent of 10^{15}cm^{-2}s^{-1} photons ($E_\gamma > 6$ eV) for the noted length of time

References. — (1) Ehrenfreund et al. (1999), (2) Gerakines et al. (1995), (3) Ehrenfreund et al. (1996)

Table 7. Percentage and column density N ($10^{17}\mathrm{cm}^{-2}$) of CO_2 ice present in each stage of processing along the line of sight: cold, warm, and segregated (due to rounding, percentages may not sum to exactly 100%).

	Cold		Warm		Segregated	
Object	% Total	N	% Total	N	% Total	N
IRAS 04016+2610	3	0.28	71	7.3	26	2.6
IRAS 04108+2803B	33	1.6	30	1.5	37	1.8
IRAS 04239+2436	10	0.57	87	4.9	2	0.14
IRAS 04361+2547	62	2.2	12	0.45	26	0.95
IRAS 04365+2535	2	0.17	61	4.9	37	2.9
DG Tau B	1	0.05	76	3.2	23	1.0
HL Tau	32	0.45	32	0.44	36	0.51
IC 2087 IR	9	0.35	68	2.8	23	0.95
L1551 IRS 5	22	1.9	54	4.6	24	2.1

Table 8. Molecular cloud and Class 0 abundances.

Source	$N(H_2O)$ (10^{18}cm^{-2}) [This work]	$N(H_2O)$ (10^{18}cm^{-2}) [Lit., (Refs)]	$N(CO_2)/N(H_2O)^{a}$ [This work]	$N(CO_2)/N(H_2O)$ [Lit., (Refs)]
CK 2 [Serpens]	2.9	3.5 (1)	0.29	0.33 (2)
Elias 13 [Taurus]	0.95	1.0 (3)	0.14	0.15,0.19 (2,5)
Elias 16 [Taurus]	2.2	2.5 (4)	0.2	0.18,0.23 (3,5)
CepE-MM	$<29.7^{b}$	···	>0.09	···
L1448 IRS2	$<28.6^{b}$	···	>0.1	···
W3(OH) + W3	···	···	···	···

[a] $N(CO_2)$ calculated using the band strength A of pure CO_2 in order to facilitate comparison with published values.

[b] Calculated from a scaled pure H_2O spectrum.

References. — (1) Eiroa & Hodapp (1989), (2) Knez et al. (2005), (3) Whittet et al. (1988), (4) Chiar et al. (1995), (5) Nummelin et al. (2001)

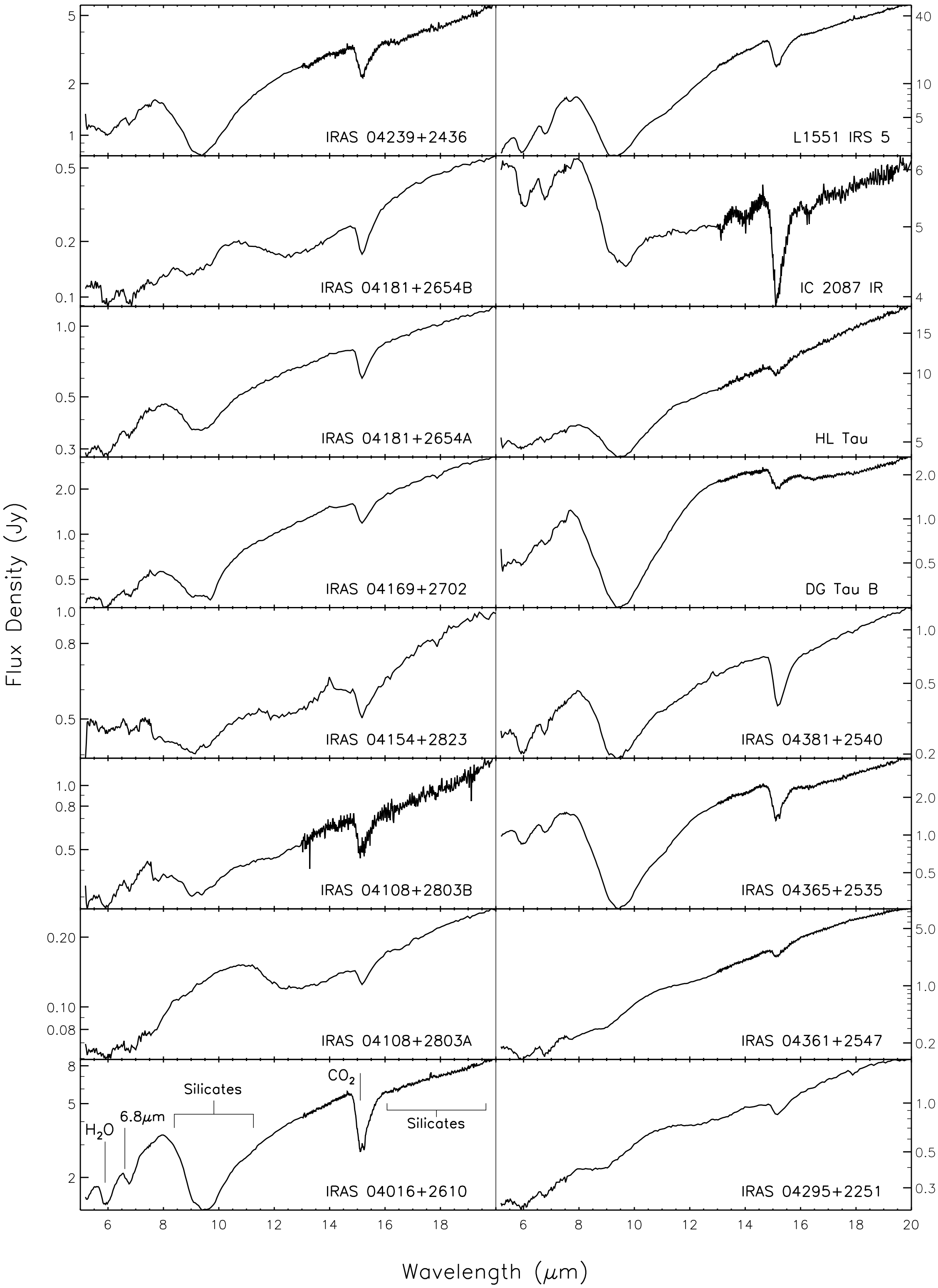

Fig. 1.— Our sample IRS spectra. The lower left object has been marked with the locations and primary carriers of the most prominent absorption features. Note that the 9.7 μm silicate feature may also appear partly or wholly in emission.

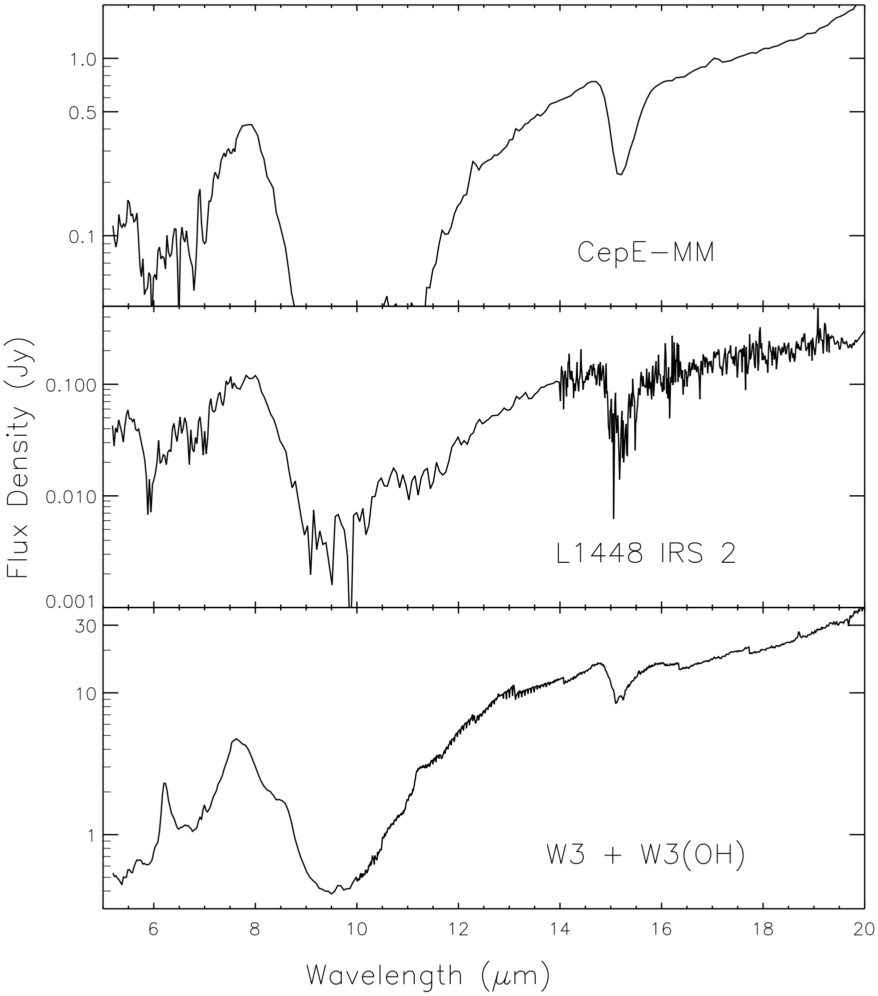

Fig. 2.— IRS spectra of the Class 0 protostars CepE-MM (in Cepheus) and L1448 LRS 2 (in Perseus), and the line of sight to W3(OH) through the W3 molecular cloud. The 9.7 μm silicate absorption feature in CepE-MM is saturated.

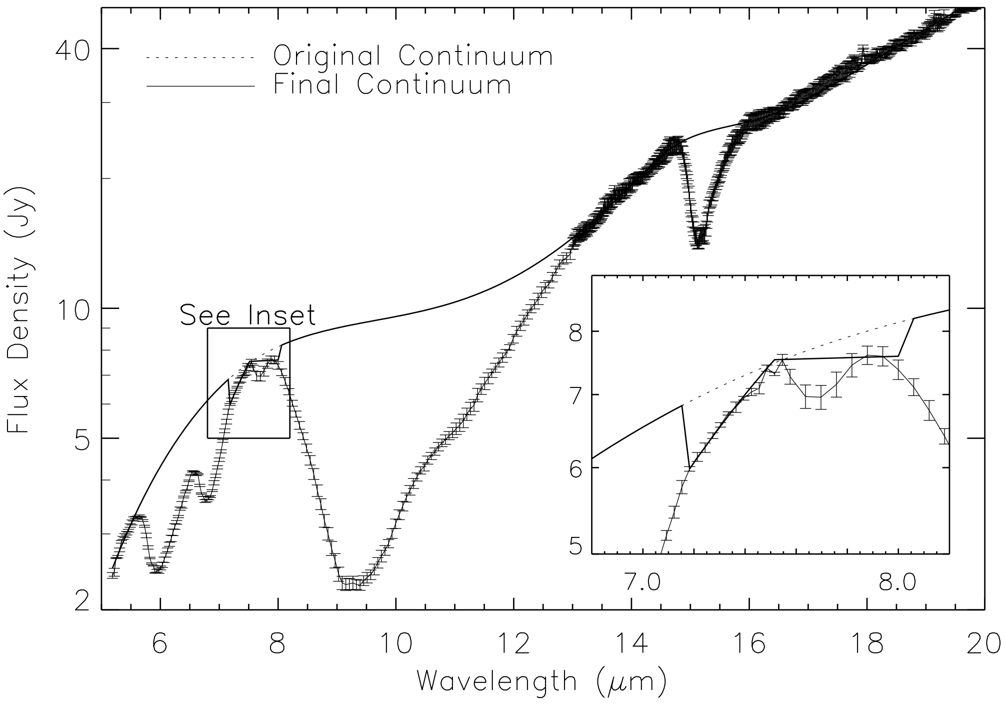

Fig. 3.— Example of the applied continuum determination using the spectrum of L1551 IRS 5. The inset shows the additional continuum imposed on the 7-8 μm range.

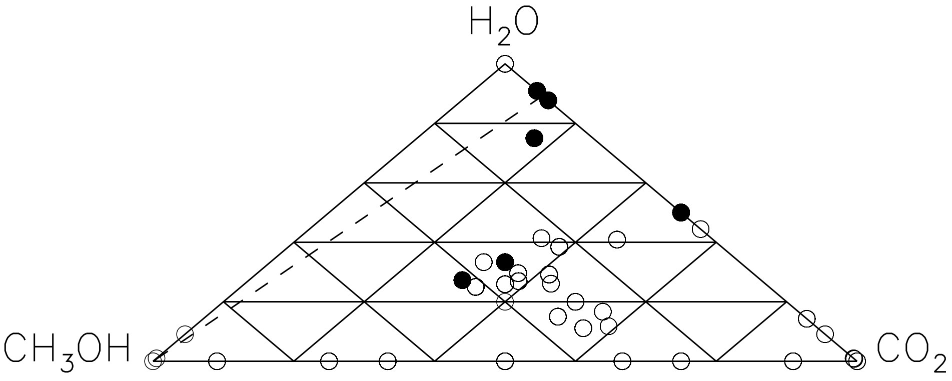

Fig. 4.— Range of non-irradiated H_2O:CH_3OH:CO_2 laboratory compositions for which there is infrared spectroscopy in the Leiden University database (all circles). The vertices represent the pure molecular ices, and distance from each molecule's vertex indicates decreasing relative abundance of that molecule (solid lines at increments of 20%). The filled circles represent mixtures whose $\tau_{6.0}/\tau_{15.2}$ ratio falls within the range spanned by the ratios from the YSO spectra (Section 4), and the dashed line indicates the compositional locus where $CO_2/H_2O=0.12$ (Section 6.1).

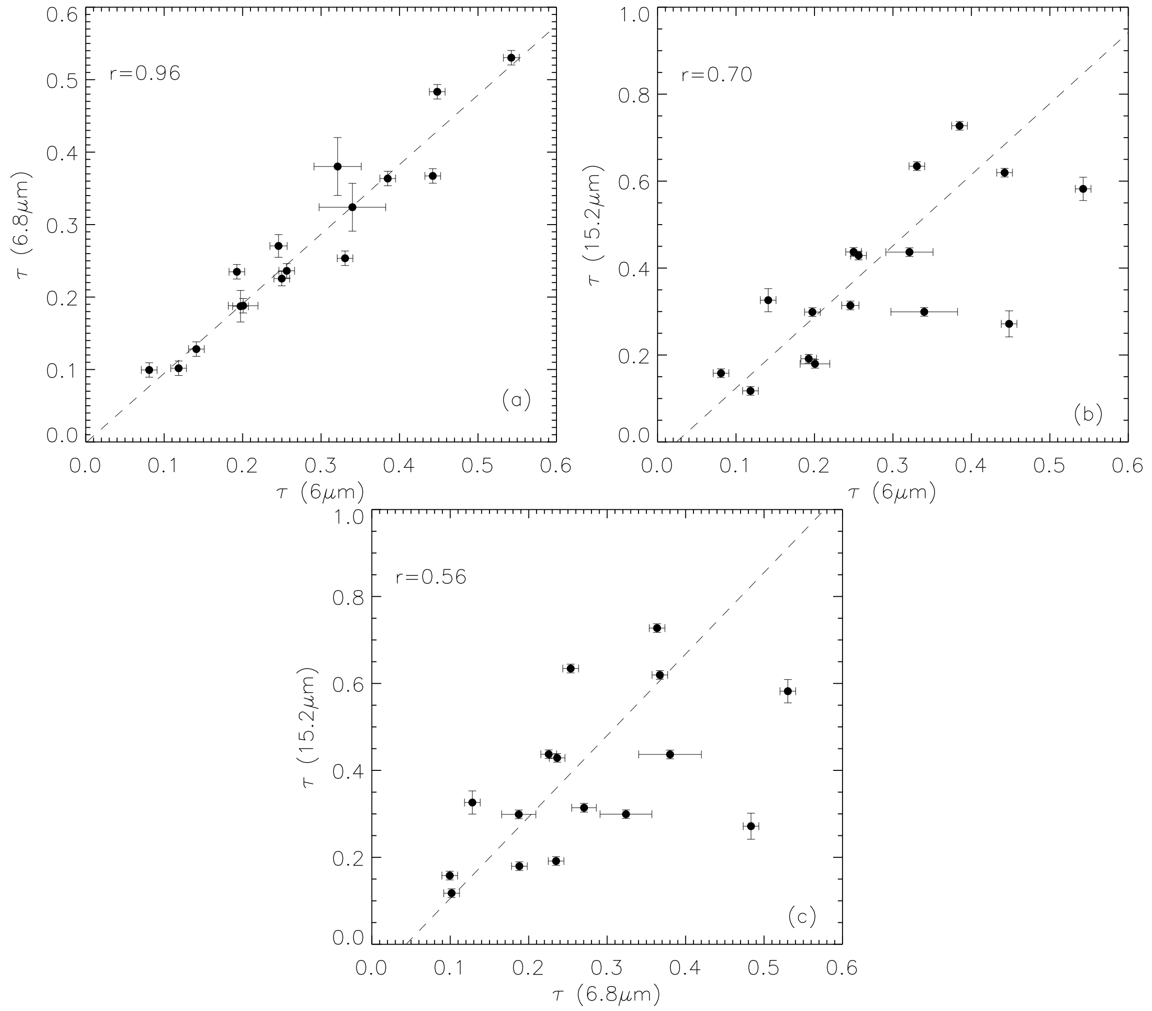

Fig. 5.— Relationships between feature peak optical depths for our low-mass YSOs. Panel (a) shows $\tau_{6.8\mu m}$ vs $\tau_{6.0\mu m}$, panel (b) shows $\tau_{15.2\mu m}$ vs $\tau_{6.0\mu m}$, and panel (c) shows $\tau_{15.2\mu m}$ vs $\tau_{6.8\mu m}$. The dashed lines indicate the best linear fit.

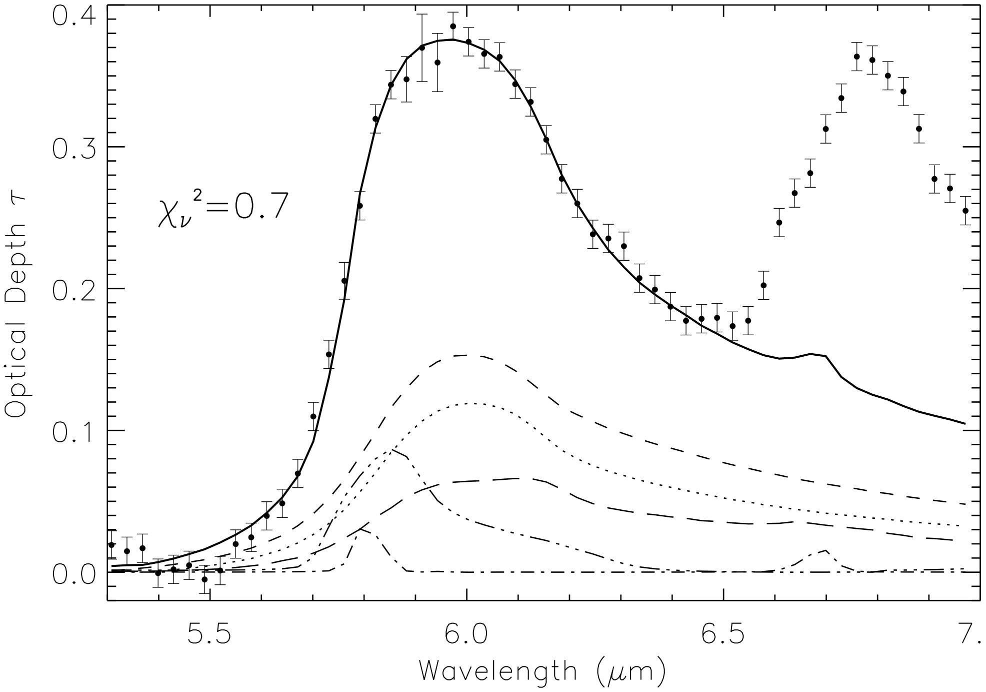

Fig. 6.— The 6 μm feature of IRAS 04016+2610, fit by a combination of pure H_2O at 10 and 50 K (dots and short dashes), pure H_2CO at 10 K (dot-dash), pure HCOOH at 10 K (dash-triple dots), and H_2O:NH_3 10:2 at 10 K (long dashes). The solid line is the sum. The 6.8 μm feature is deliberately excluded from the fit.

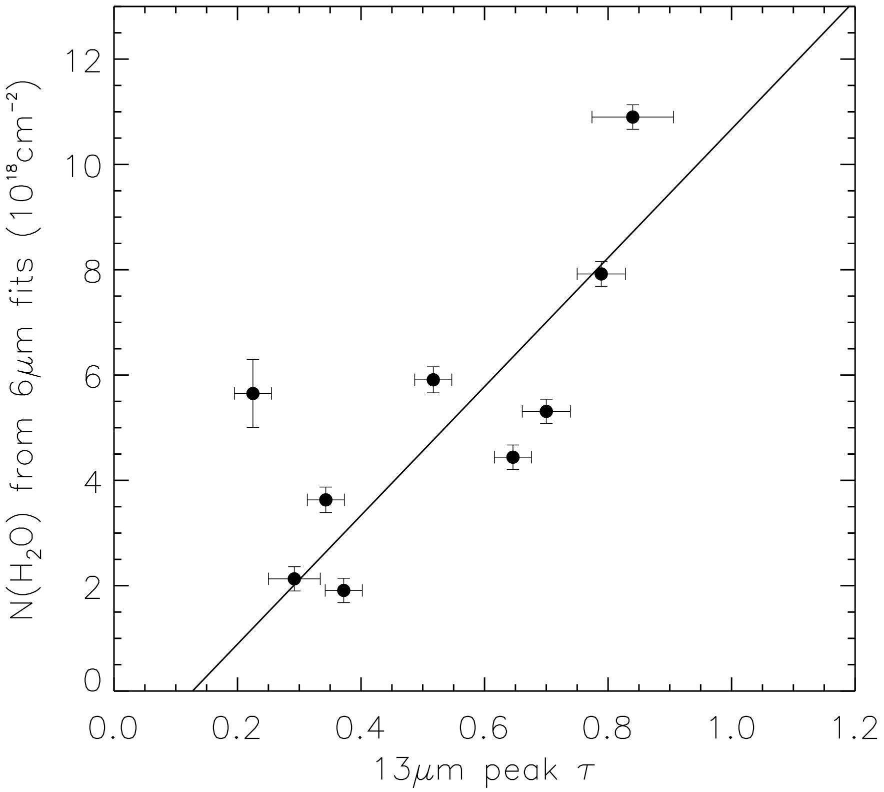

Fig. 7.— Peak optical depth in the water ice libration mode ($\lambda \sim 13$ μm), plotted against the water ice column density $N(\mathrm{H_2O})$ derived from the 6 μm water ice feature as described in Section 5.1.1. Points and uncertainties are results for the nine Taurus objects in which the 9.7 μm silicate features are strongly in absorption.

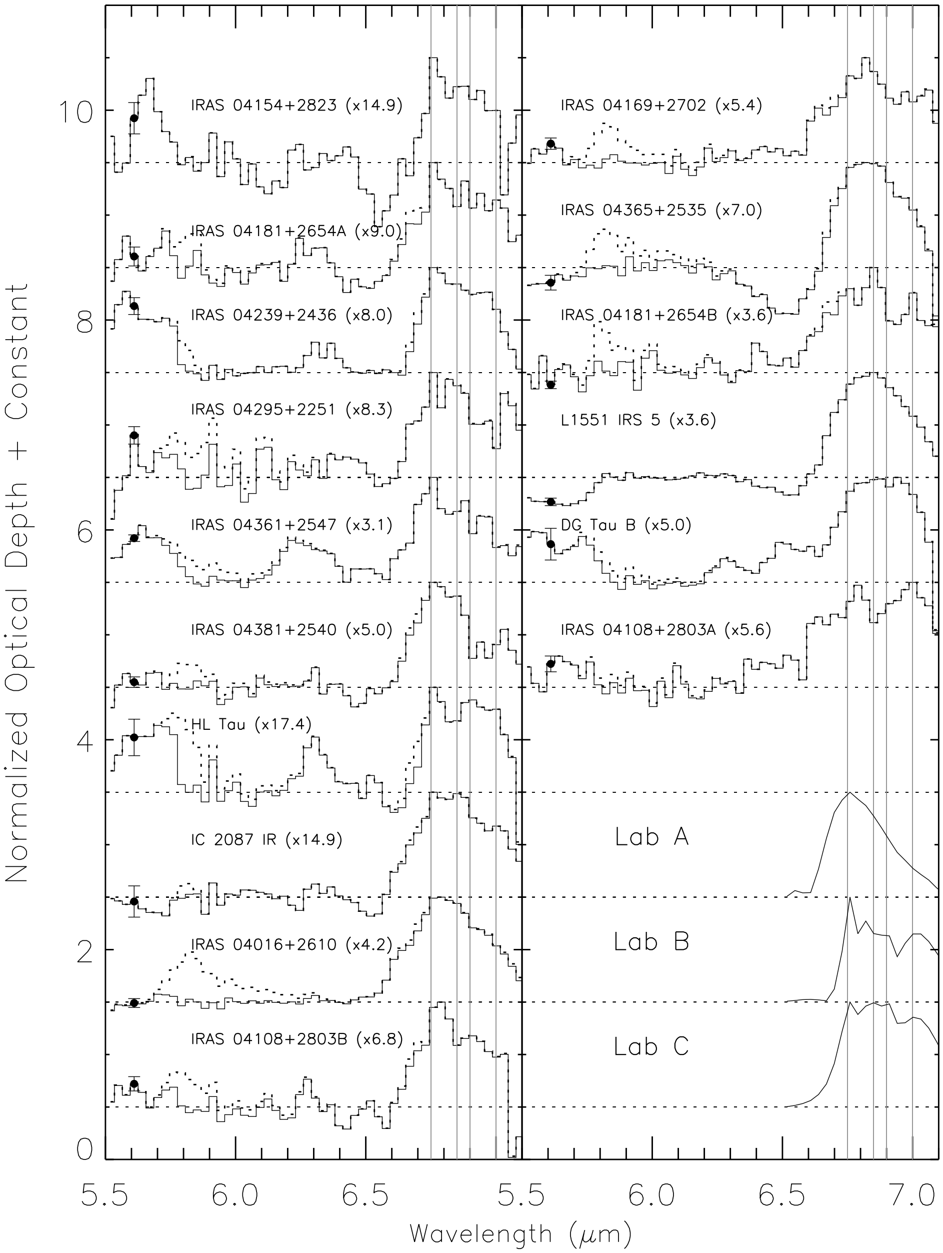

Fig. 8.— The sample's 6-7 μm profiles (after subtraction of the H_2O contributions (dashed) and all contributions (solid) at 6 μm) normalized to 1 and shifted vertically, sorted by 6.8 μm peak position (the point near 5.6 μm indicates the approximate optical depth uncertainty). The 5.6-5.7 μm residuals are almost entirely byproducts of continuum mismatches. Also shown for comparison are normalized laboratory spectra—*Lab A*: H_2O:CO:NH_3 10:2.5:2 at 165 K (irradiated to create NH_4^+), *Lab B*: H_2O:CH_3OH:CO_2 9:1:2 at 10 K, *Lab C*: H_2O:CH_3OH 1:100 at 10 K.

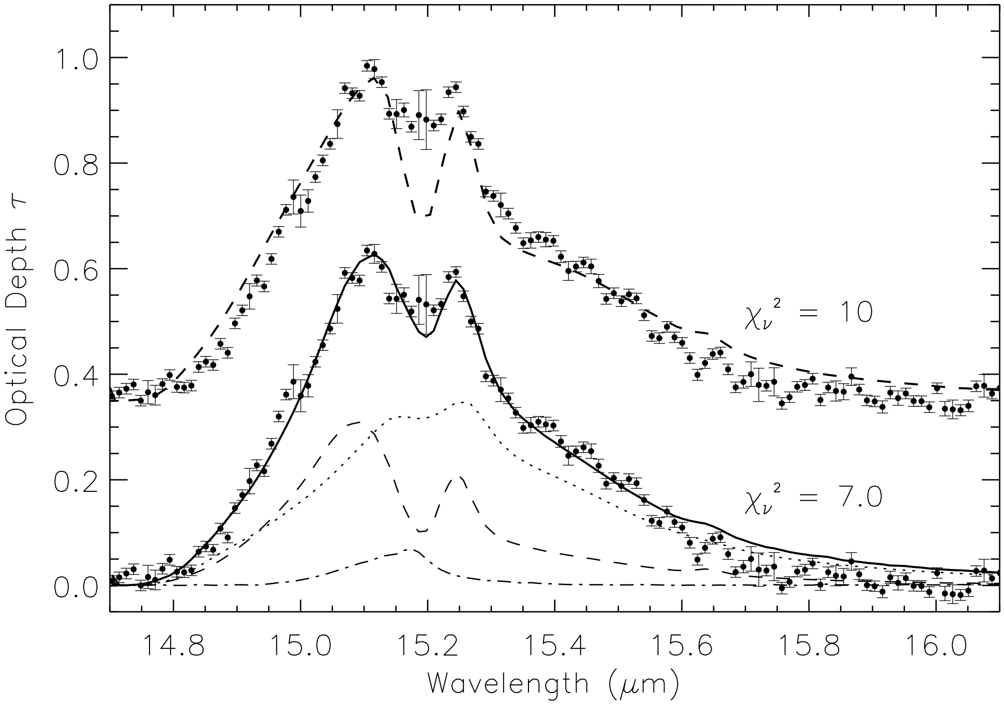

Fig. 9.— 15.2 μm feature of IRAS 04365+2535, shown repeated with a vertical offset. The spectrum on the bottom is overlaid with a fit of H_2O:CH_3OH:CO_2 0.9:0.3:1 at 98 K (dots), H_2O:CH_3OH:CO_2 1:1:1 at 130 K (dashes), and CO:H_2O 10:1 at 30 K (dash-dot). The solid line is the sum. The heavy dashed fit on the upper spectrum is a fit using only H_2O:CH_3OH:CO_2 1:1:1 at 118 K. The excess between 14.95 and 15 μm is due to gas-phase CO_2 ro-vibrational ν_2 Q-branch lines, blended together at this resolution.

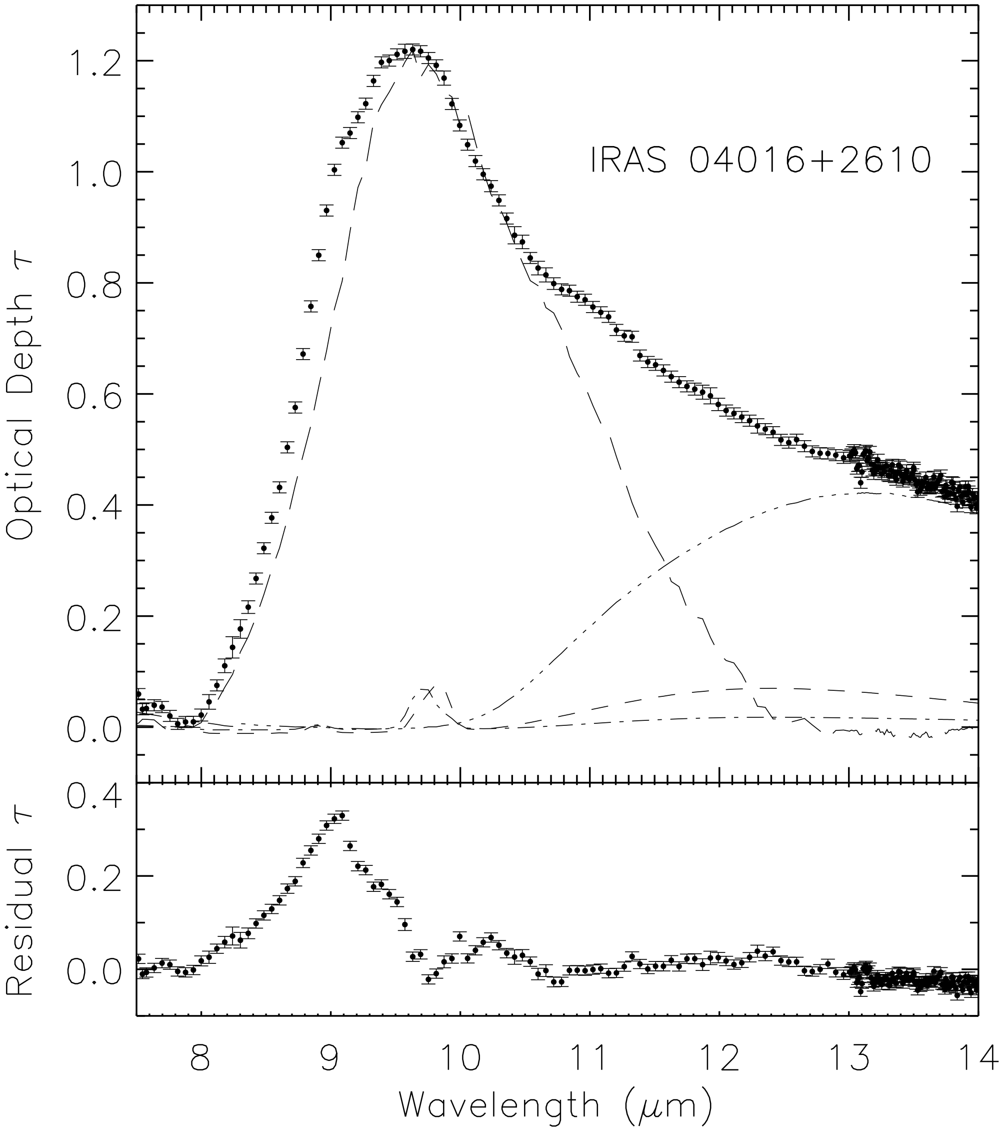

Fig. 10.— Model of the absorption around 10 μm in IRAS 04016+2610. Shown are the observed data (points), the GCS 3 silicate profile (long dashes; Kemper et al. 2004), pure water ice at 10 K (dash-triple dots), and the two methanol-bearing mixtures described in Section 5.4 and listed in Table 6 (short dashes and dot-dashes), scaled per this object's 15.2 μm fit. The remnant peak at 9 μm is likely NH_3 ice. The model and observation are consistent with one another in the relevant wavelength range.

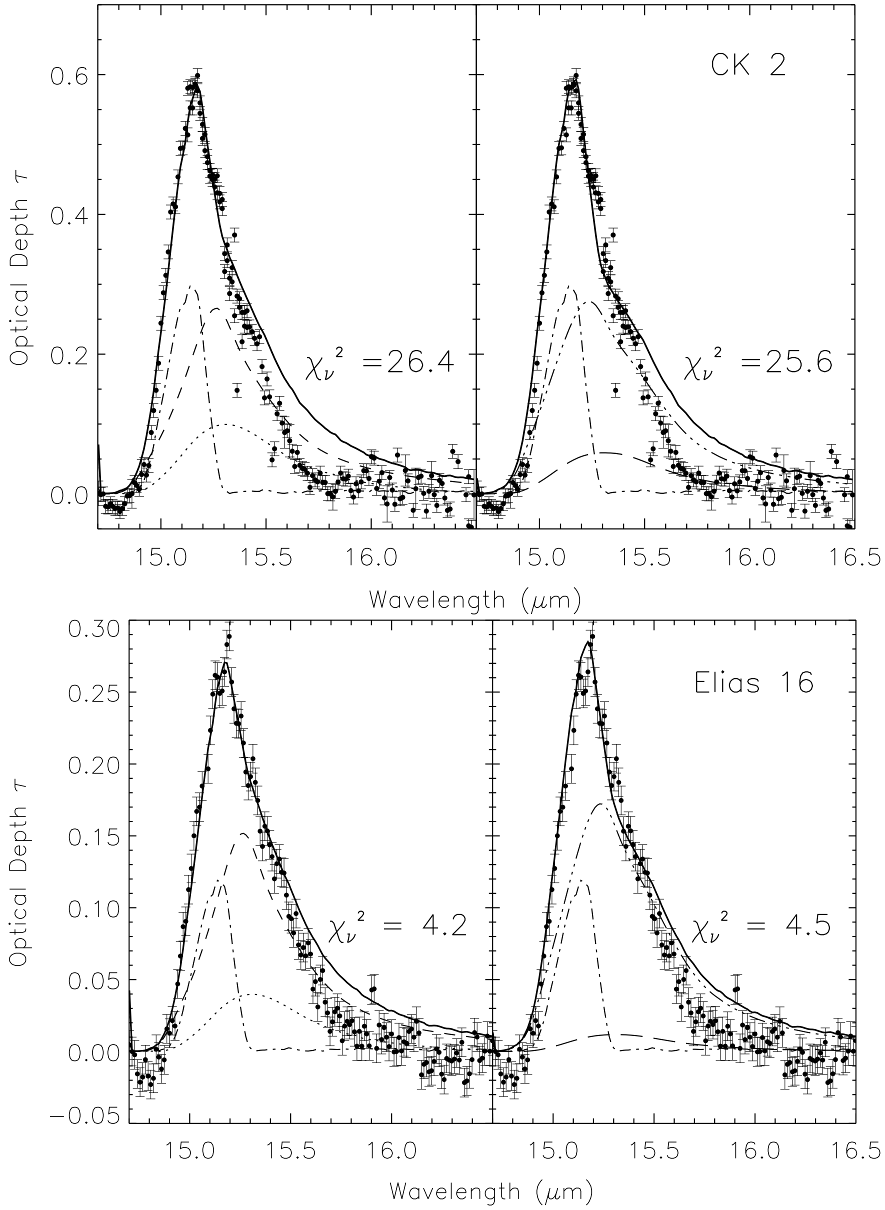

Fig. 11.— Comparison of fits to the Serpens background star CK 2 (top) and Taurus background star Elias 16 (bottom). The left panels are repeats of the fits by Knez et al. (2005), where the dotted line is a laboratory spectrum of H_2O:CO_2 10:1 at 10 K, the dashed line is H_2O:CO_2 1:1 at 10 K, and the dash-dot line is CO:N_2:CO_2 10:5:2 at 30 K. The mismatch on the red wing is caused by the forced continuum at ∼16.5 μm, which ignores the extent of some of the ice feature wings as measured in the laboratory. In the right panels, the dash-dot line is the same, but the H_2O:CO_2 10:1 spectrum has been replaced with H_2O:CH_3OH:CO_2 9:2:1 at 30 K (long dashes) and the H_2O:CO_2 1:1 with H_2O:CH_3OH:CO_2 0.9:0.3:1 at 30 K (dash-triple dot).

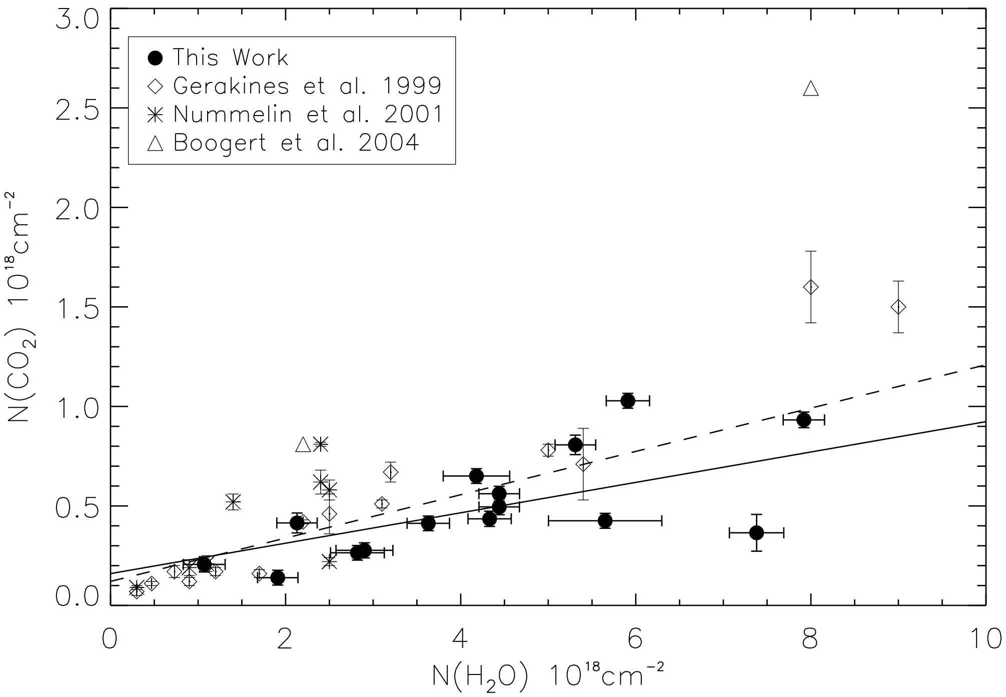

Fig. 12.— Correlation between solid $N(H_2O)$ and $N(CO_2)$ for many different lines of sight. Our sample comprises low-mass protostars, Gerakines et al. (1999) contains mostly massive protostars and some galactic center sources, Nummelin et al. (2001) comprises low- and high-mass YSOs as well as some molecular cloud sight-lines, and Boogert et al. (2004) contains two low-mass protostars. The solid line is the ratio between column densities using only the current work's sample, and the dashed line is the ratio using all objects except the upper outlier from Boogert et al. (2004). Note that this work uses a CO_2 band strength (at 15.2μm) $\sim$36% higher than that of the previous studies, which may account for most of the difference in $N(CO_2)/N(H_2O)$.

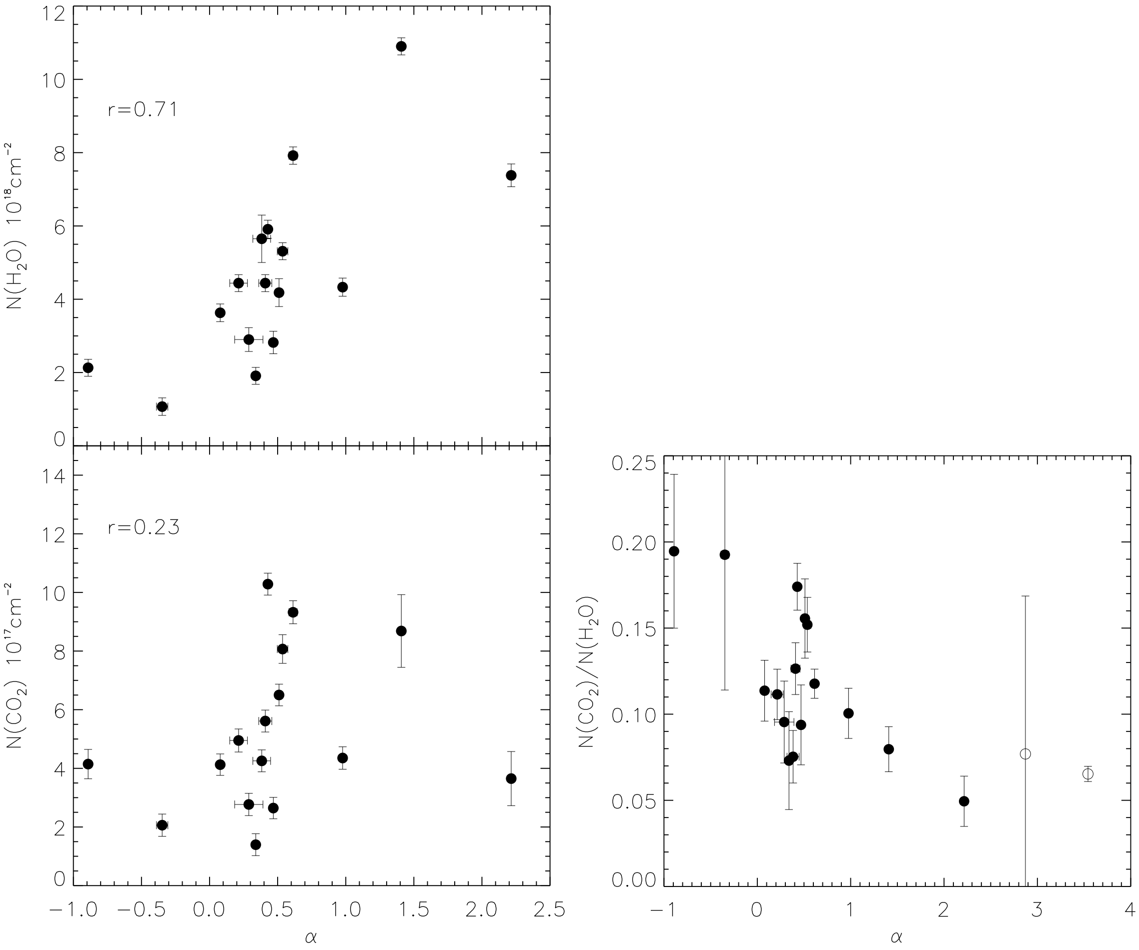

Fig. 13.— Relationships between the SED spectral index (α; 7-30 μm) and $N(\mathrm{CO_2})$, $N(\mathrm{H_2O})$, and $N(\mathrm{CO_2})/N(\mathrm{H_2O})$. The filled circles represent our Class I/II data, and the open circles represent the Class 0 objects.

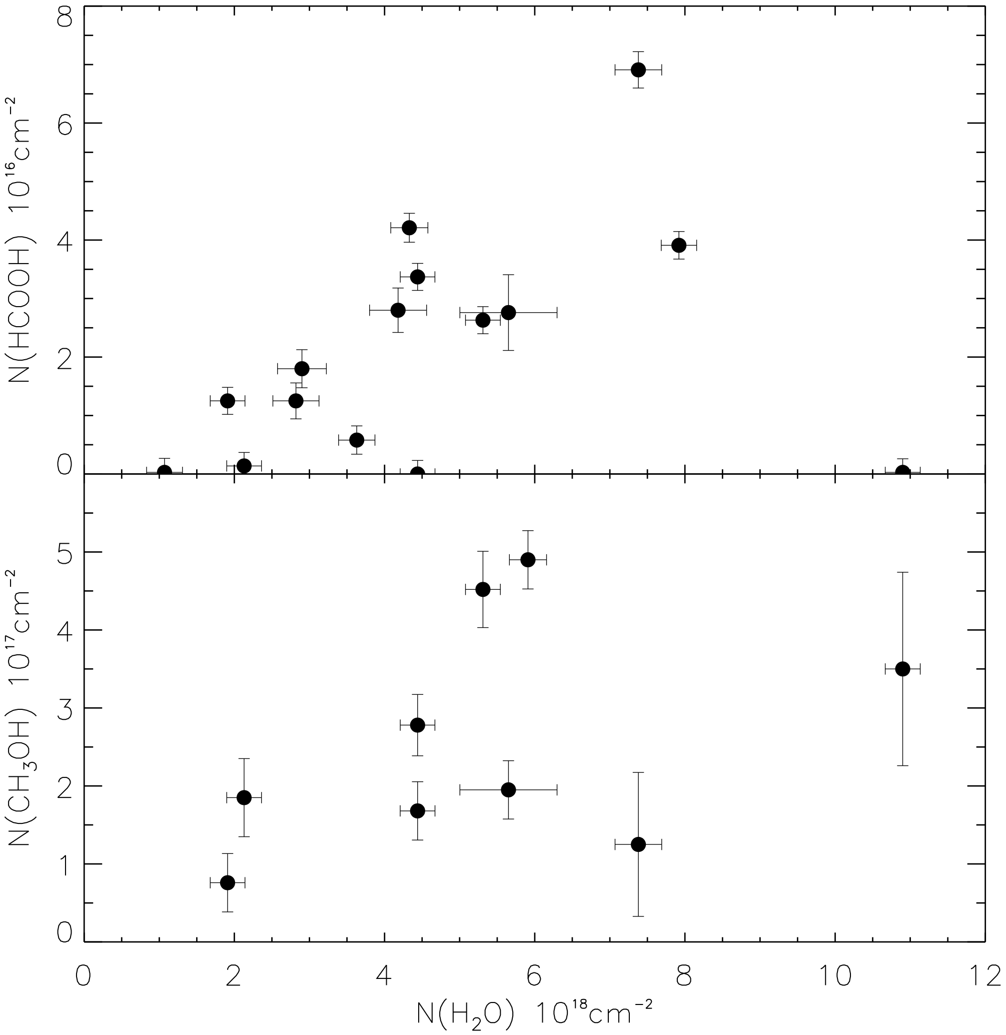

Fig. 14.— Ratios between $N(\mathrm{H_2O})$, and $N(\mathrm{HCOOH})$ and $N(\mathrm{CH_3OH})$, for the Class I/II sample (Section 6.1). The bottom plot refers to $N(\mathrm{CH_3OH})$ embedded in a $\mathrm{H_2O{:}CO_2}$ matrix.

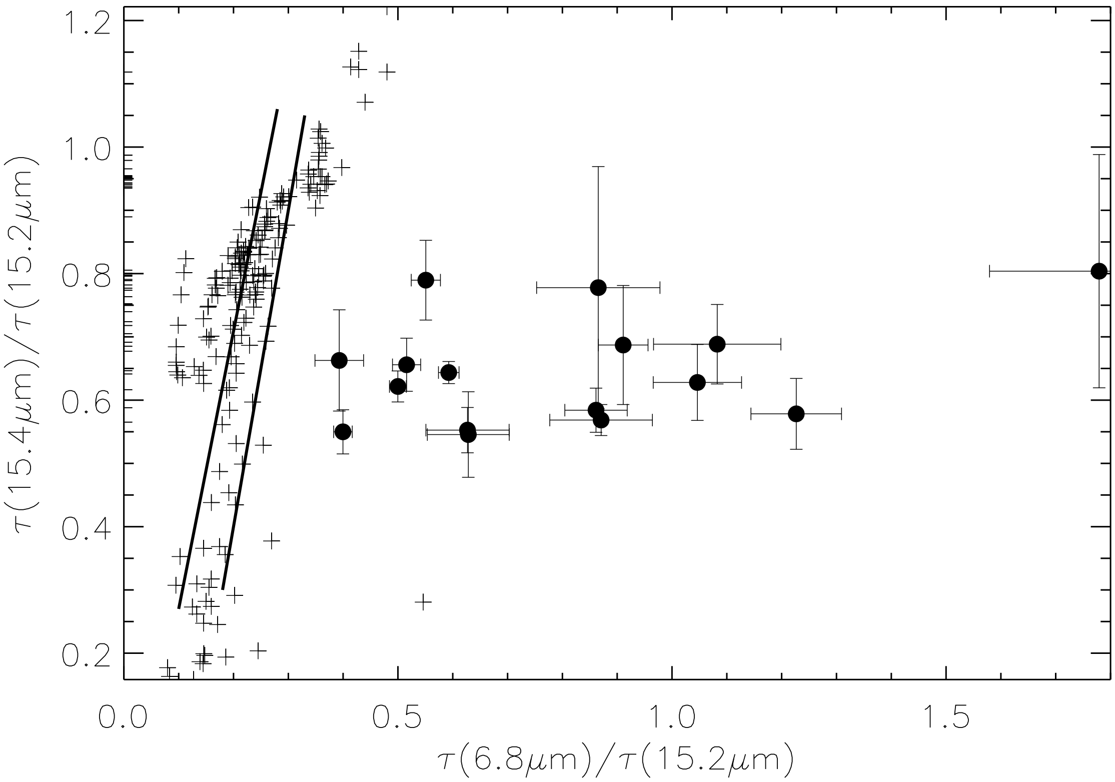

Fig. 15.— The correlation between 6.8 μm and 15.4 μm optical depths in the laboratory ice spectra (plus signs) and the observed YSO spectra (solid circles). Both have been scaled by peak 15.2 μm optical depth. The laboratory data cover temperatures from 10-185K and CH_3OH/CO_2 abundance ratios of 0-1.4, which are roughly indicated by the solid lines: [$\lesssim$0.5] / [0.5-1.4] / [$\gtrsim$1.4]. The vertical spread depends largely on temperature, with warmer mixtures of a constant composition showing weaker 15.4 μm shoulders.

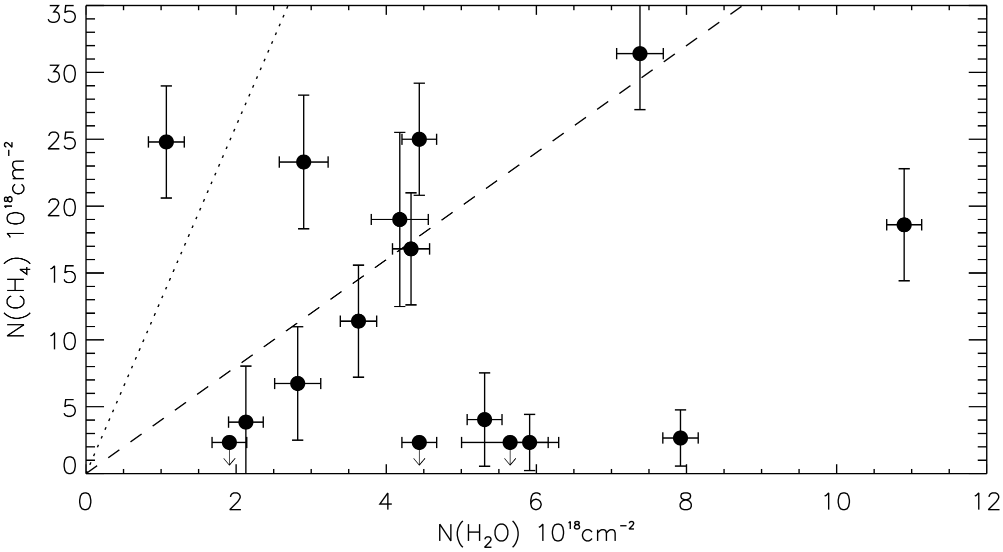

Fig. 16.— Comparison of solid $N(H_2O)$ and $N(CH_4)$ for the YSO sample. The dashed line indicates the maximum of ∼4% (CH_4 relative to H_2O) observed towards massive protostars (e.g. Gibb et al. 2004), and the dotted line is the newer 13% maximum reported by Öberg et al. (2008) towards low-mass protostars.

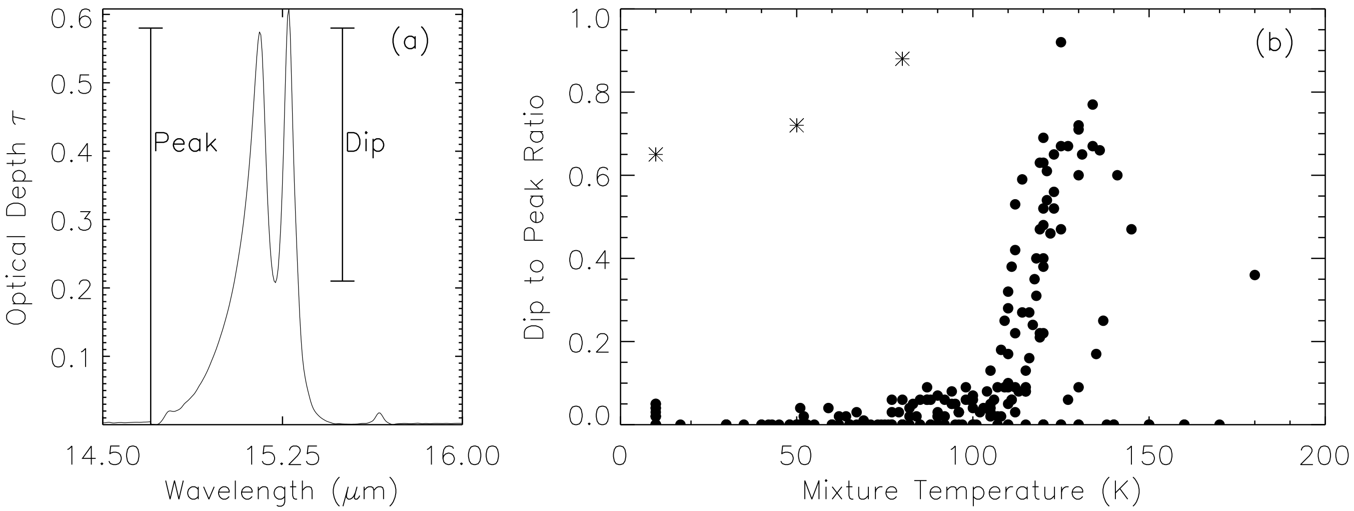

Fig. 17.— The "dip-to-peak" ratio as a measure of the amount of CO_2 segregation. *(a)*—Demonstrates how the values were measured for each laboratory ice spectrum, using pure CO_2 as an example. *(b)*—The relative dip strength as a function of laboratory ice temperature, showing the rapid onset of the process near ∼105 K. Much of the scatter in (b) is due to the dependence of CO_2 segregation temperature on the exact composition of the matrix in which it is embedded. The large asterisks in the upper left represent pure CO_2 ice.

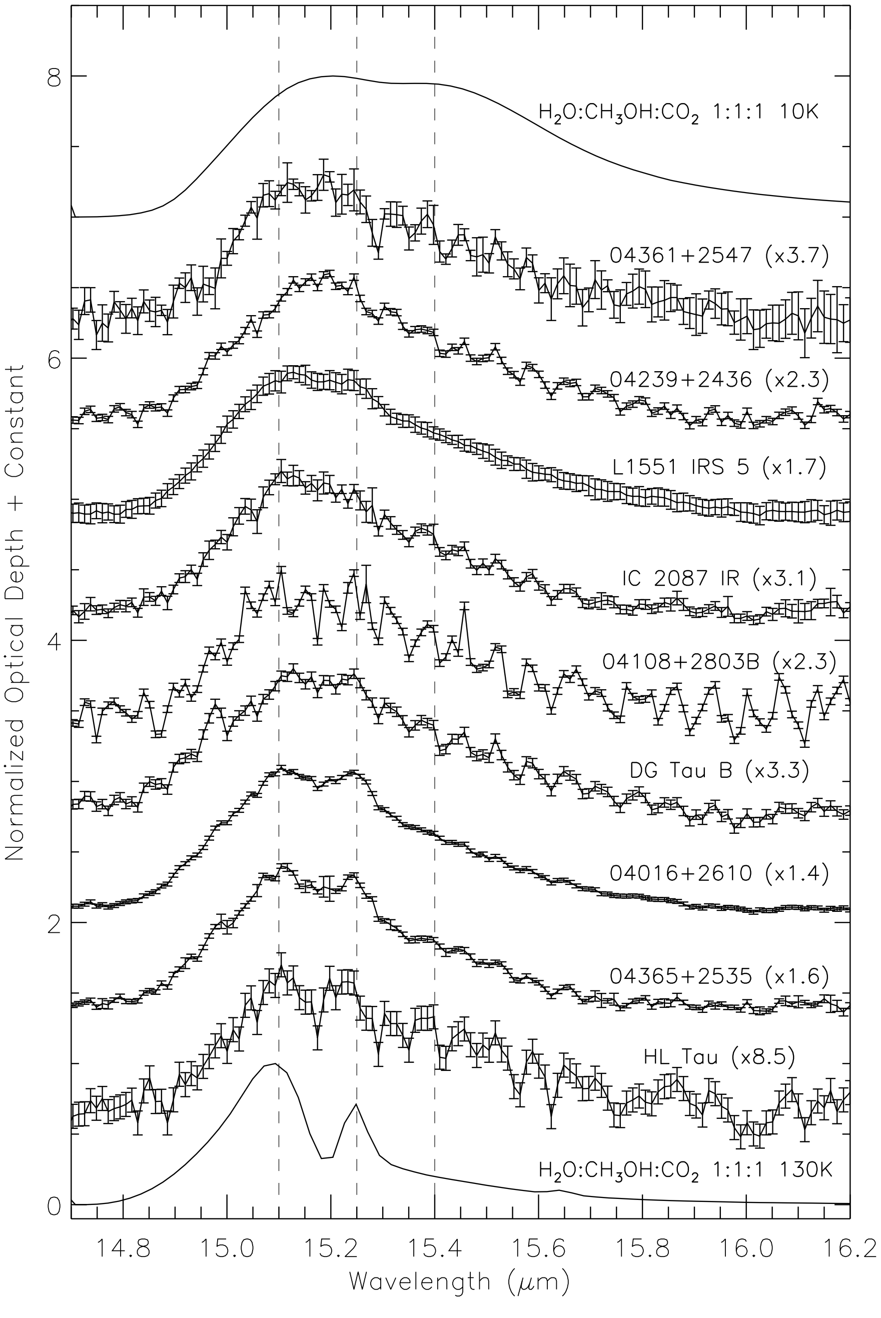

Fig. 18.— The high-resolution 15 μm Class I/II profiles visually ordered by "peakiness," normalized to 1, and vertically offset for clarity. The dotted lines at 15.1 and 15.25 μm mark the peak positions of pure CO_2, and the one at 15.4 μm indicates the $CH_3OH:CO_2$-complex shoulder. The top and bottom spectra are laboratory mixtures as indicated.

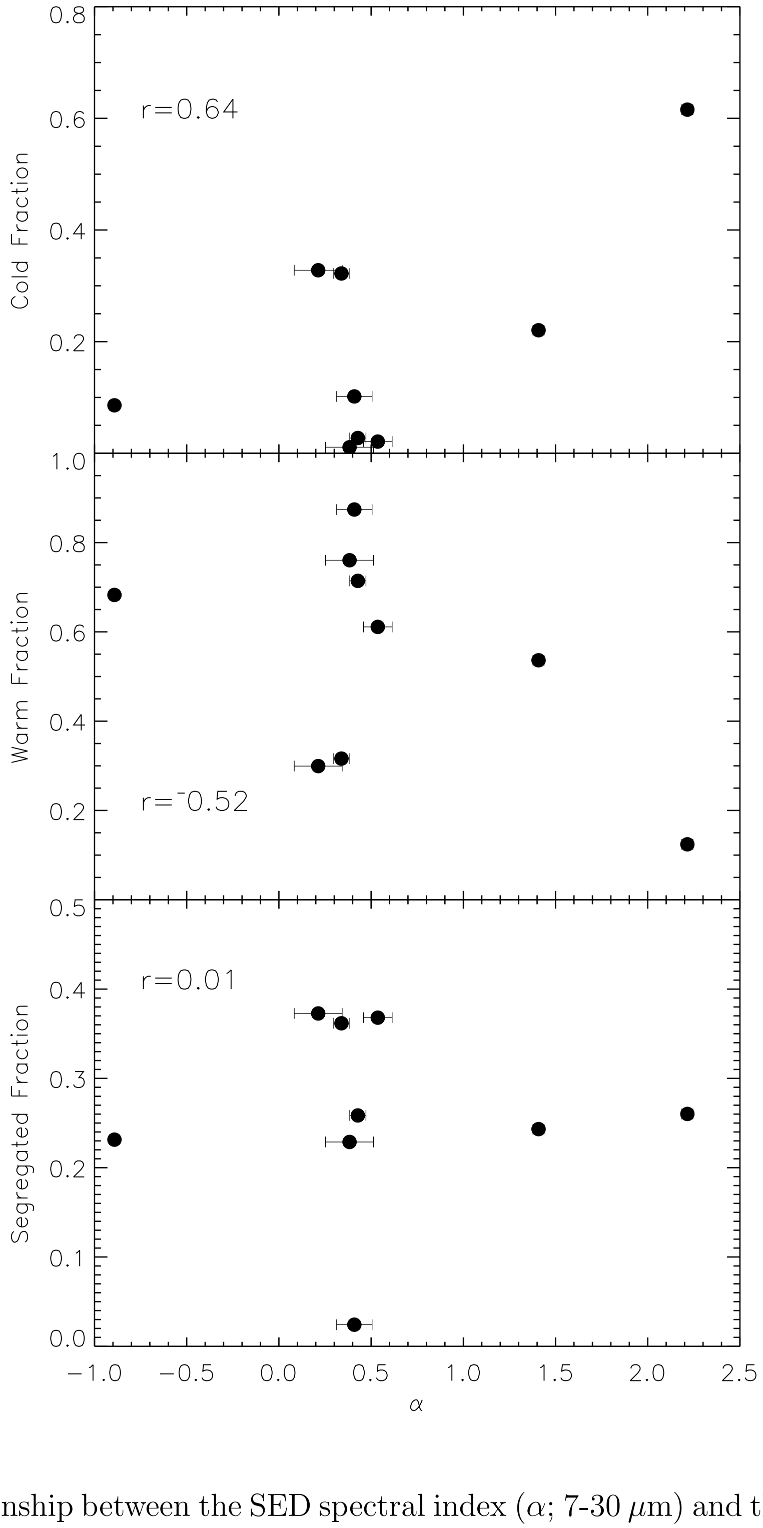

Fig. 19.— Relationship between the SED spectral index (α; 7-30 μm) and the CO_2 processing fractions in our Class I/II sample.

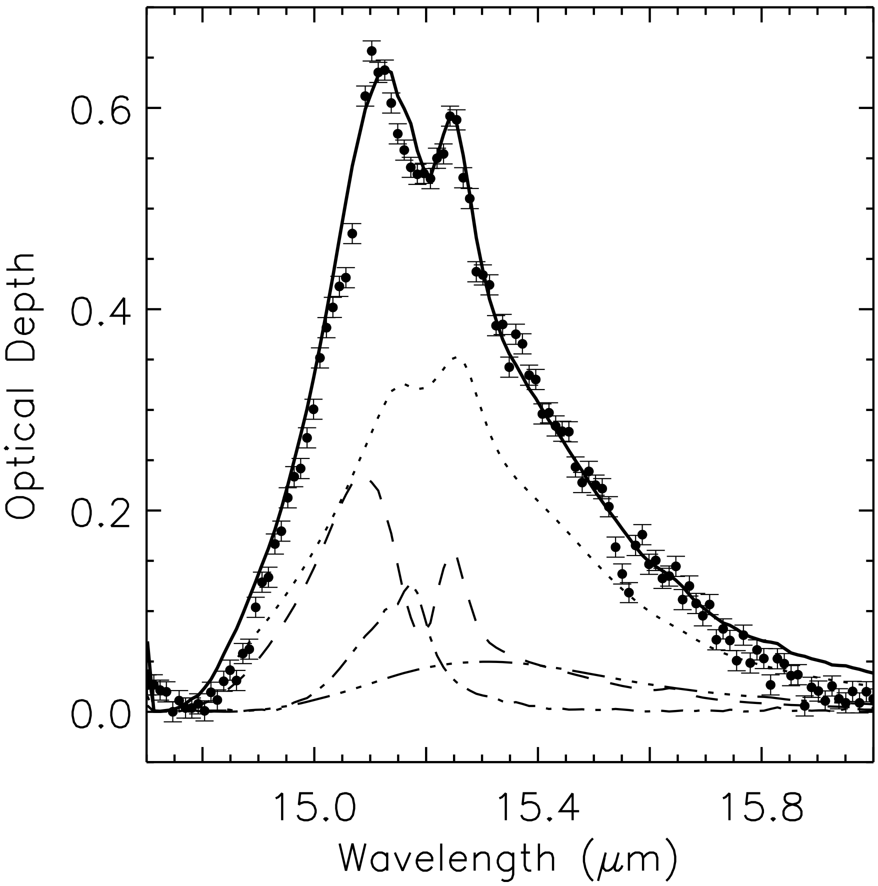

Fig. 20.— 15.2 μm CO_2 feature probing W3(OH) and the foreground W3 cloud. It has been fitted with a combination of H_2O:CH_3OH:CO_2 0.9:0.3:0.1 at 98 K (dotted line), H_2O:CH_3OH:CO_2 1:1:1 at 130 K (dashed line), CO:H_2O at 10:1 at 30 K (dot-dashed line), and H_2O:CO_2 10:1 at 10 K (dash-triple dot). The solid line is the sum.